Details of human middle ear morphology based on micro-CT imaging of PTA stained samples

Details of human middle ear morphology based on micro-CT imaging of PTA stained samples

De Greef Daniel[a,*], Buytaert Jan A.N.[a], Aerts Johan R.M.[a], Van Hoorebeke Luc[b], Manuel Dierick[b], Dirckx Joris[a]

[a] Laboratory of Biomedical Physics, University of Antwerp, Groenenborgerlaan 171, 2020 Antwerp, Belgium

[b] UGCT - Department of Physics and Astronomy, Ghent University, Proeftuinstraat 86, 9000 Ghent, Belgium

Abstract

A multitude of morphological aspects of the human middle ear (ME) were studied qualitatively and/or quantitatively through the post-processing and interpretation of micro-CT (micro X-ray computed tomography) data of six human temporal bones. The samples were scanned after phosphotungstic acid (PTA) staining to enhance soft-tissue contrast. The influence of this staining on ME ossicle configuration was shown to be insignificant. Through post-processing, the image data were converted into surface models, after which the approaches diverged depending on the topics of interest. The studied topics were: the ME ligaments; morphometric and mechanical parameters of the ossicles relating to inertia and the ossicular lever arm ratio; the morphology of the distal incus; the contact surface areas of the tympanic membrane and of the stapes footplate; and the thickness of the tympanic membrane, round window of the cochlea, ossicle joint spaces and stapedial annular ligament. Some of the resulting insights are relevant in ongoing discussions concerning ME morphology and mechanical functions, while other results provide quantitative data to add to existing data. All findings are discussed in the light of other published data and many are relevant for the construction of mechanical finite element simulations of the ME.

Keywords (3-6): Middle ear; Micro-CT; Staining; Ligaments; Distal incus; Ossicles.

[*]**Corresponding author**
Email address: daniel.degreef@uantwerpen.be
URL: www.uantwerp.be/bimef
Phone number: +32 (0)3 265 34 35

1. Introduction

The mammalian middle ear (ME) conducts acoustic signals entering the external ear to the cochlea in the inner ear. Through various mechanisms, the ME collects and amplifies the pressure of the incident sound waves before transmitting them to the cochlea, in order to match the acoustic impedances of outside air and cochlea fluid. Human ME morphology has been a focal point in otologic research in the past and the present (e.g. (Kirikae, 1960; Fleischer, 1978; Gulya and Schuknecht, 1995; Hemila et al., 1995)). However, there still remain a number of topics where no consensus has been reached, either in terms of shape, volume, point of attachment, spatial coordinates, material properties, inter-individual variability or even tissue type. The challenge of fully understanding ME functionality is made considerably more difficult by the presence of many different tissue types, both generic and specialized, in the ME, and their delicate interfaces and interactions.

Knowledge on ME morphology is especially relevant for two otologic fields of study. First, it is important for the construction of highly realistic finite element models (FE models) of ME mechanics, a research branch that is very popular in the field (Funnell and Laszlo, 1978; Funnell and Medical, 1983; Williams and Lesser, 1990; Wada et al., 1992; Kelly et al., 2003; Fay et al., 2006; Gan et al., 2006, 2009; Wang et al., 2007; Hoffstetter et al., 2010; Gentil et al., 2014; Volandri et al., 2011, 2012; Gentil et al., 2011; Aernouts et al., 2012; Böhnke et al., 2013; Muyshondt et al., 2014; De Greef et al., 2014; Gan and Wang, 2014). Secondly, new data and statistical knowledge about these structures are of direct relevance to the field of otologic surgery, for example for surgical interventions or for the implantation of hearing aids.

The present work covers a range of topics in ME morphology, studied through micro-CT measurements of six stained human samples. The study of each topic serves one of the two following purposes: either it brings clarification to a topic which has been a subject of confusion, inconsistency and debate in the past; or it confirms or at least adds to quantitative data and properties on a topic about which a consensus already exists but can benefit from additional numerical data. Each of the topics has a subsection in ‘Materials and methods’, ‘Results’, and ‘Discussion’. The research questions of the topics are:

- What is the influence of the PTA (phosphotungstic acid) staining on the angles of the incudomallear joint and the incudostapedial joint?
- ME ligaments: how many do exist; what is their prevalence, location of attachment, thickness and apparent/presumed importance?
- Ossicle parameters and dimensions: what are the total volume and mass of each ossicle; what are the (relative) volume, mass and mechanical influence of the intertrabecular spaces of the ossicles; what are the coordinates of the center of mass, the values of the principal moments of inertia and the directions of the principal axis of rotation of the ossicles; what is the efficiency of rotation of the incudomallear complex around the classic anatomical axis, defined by the tip of the anterior process of the malleus and the posterior tip of the short process of the incus; what are the values of the ossicular lever arm lengths and other important morphometric dimensions?
- Morphology of the distal incus: what is the nature and what are the dimensions of the pedicle (also sometimes called strut or stem) of the lenticular process at the distal end of the incus; is there a 4^{th} ossicle?

- Surface area of the tympanic membrane (TM) and the stapes footplate: what are the values for TM and footplate surface areas as well as their ratio, i.e. the hydraulic ratio of the ME?
- What are the thicknesses of the TM, ossicle joints, stapedial annular ligament and the round window of the cochlea?

Table 1. *List of frequently used abbreviations*.

Middle ear structures (except ligaments)	
IMC	Incudomallear complex
IMJ	Incudomallear joint
ISJ	Incudostapedial joint
ME	Middle ear
RW	Round window (of the cochlea)
SAL	Stapedial annular ligament
SFP	Stapes footplate
TM	Tympanic membrane
Middle ear ligaments	
AML	Anterior mallear ligament
M-AML	Medial anterior mallear ligament
S-AML	Superior anterior mallear ligament
LML	Lateral mallear ligament
PML	Posterior mallear ligament
A-SML	Anterior superior mallear ligament
P-SML	Posterior superior mallear ligament
MIML	Medial incudomallear ligament
PIL	Posterior incudal ligament
MIL	Medal incudal ligament
LIL	Lateral incudal ligament
SSL	Superior stapedial ligament
DML	Discomallear ligament
SpML	Sphenomandibular ligament
Technical terms	
CT	Computed tomography
FE	Finite element
LSFM	Light sheet fluorescence microscopy
MRI	Magnetic resonance imaging
OCT	Optical coherence tomography
PTA	Phosphotungstic acid
Mechanical or anatomical parameters	
AnAx	Anatomical axis (AML - PIL)
COM	Center of mass
f_n	Natural frequency
PAR	Principal axis of rotation
PMI	Principal moment of inertia
r_{eff}	Efficiency ratio of the IM complex

2. Materials and methods

2.1 PTA-stained Micro-CT

Six fresh human temporal bone samples were obtained from Cochlear Technology Centre Belgium. The temporal bones were separated from the cadaver within 48h post mortem and frozen immediately afterwards. After transportation, the temporal bones were defrosted and further reduced using a saw, surgical scissors and a dental drill in size to allow for an optimal scanning resolution. The resulting samples were approximately 25 x 25 x 25 mm^3. While middle and inner ear structures were kept intact during these manipulations, mastoid cell damage was unavoidable to sufficiently reduce the sample size. The samples were then preserved in a 4 wt. % solution of formaldehyde in water (formol) until further transportation.

A first micro-CT scan - without contrast-enhancement through staining - of all samples was made at the Centre for X-ray Tomography of the Ghent University (UGCT) facility (Masschaele et al., 2007). Before the scans, the samples were rinsed by submerging them for a short time in a 100 % saline solution. During scanning, the samples were not submerged in a liquid but were kept in a closed plastic container with a layer of water at the bottom to provide atmospheric saturation, as a measure to minimize tissue dehydration effects during the scan. For each sample, scanning parameters were iteratively optimized to maximize image quality for segmentation purposes. For this, UGCT relies on an in-house developed evaluation tool that calculates X-ray transmissions based on Monte-Carlo simulations of the X-ray source and detector, for different inputs like sample size and composition, kV setting, filtration etc. The resulting dataset of the scans had an isotropic voxel pitch of 22.8 μm (samples 1, 3-6) and 18.5 μm (sample 2).

For the second scan, contrast-enhancing staining was applied using phosphotungstic acid (PTA) to enhance the visibility of soft tissue structures in the samples. One opening of approximately 4x4 mm^2 was drilled in the tympanic cavity wall of each sample and the samples were submerged in a 3 wt. % solution of PTA in water. For a short period of time, the PTA-solution with the submerged sample was kept in a decreased pressure environment, to allow air to escape from the middle ear cavity through the opening and thereby enable an optimal penetration of the PTA-solution in the middle ear cavity. Then, the sample was kept for 48 hours in the solution to obtain sufficient absorption of the staining agent by the soft tissue middle ear structures. Afterwards, the samples were rinsed in saline once more, with the purpose of extracting any excessively absorbed staining agent. Finally, the samples were scanned again at the UGCT facility.

2.2 Segmentation

After 2D-reconstruction of the micro-CT scans, every dataset was segmented using Amira® 5.3 (FEI Visualization Sciences Group). This was performed using a combination of automatic and manual segmentation tools. A first distinction between separate structures was made by threshold-based region growing starting from a user-defined point. However, despite the sample staining, this semi-automatic segmentation technique proved insufficient to detect all boundaries between components, especially between adjacent soft-tissue structures. Significant manual input and sometimes a-priori knowledge of the ME anatomy was required in order to distinguish all structures. Therefore, in a second stage, all cross-sections were visually inspected and improved with manual and semi-automatic segmentation tools and algorithms such as paint brush, hole-filling, interpolation etc. The segmentation process resulted for each dataset in a ‘label’ dataset with the same

dimensions as the 3D CT image-stack, containing for each voxel the anatomical structure that was assigned to it by the operator. For most post-processing purposes, the label data needed to be converted into geometrical surface models, described by a number of contiguous triangles, through a triangulation algorithm in Amira®.

2.3 Approach per Topic

After acquiring the micro-CT data and performing the image segmentation, the next analytical steps were determined by the different studied topics, depending on the respective goal and research question. This section describes the strategic approach per topic.

Topic I: Influence of PTA on Ossicle Configuration

If the used PTA staining alters the spatial configuration of the ossicles significantly and systematically, the relevance of most other results in this study could be questioned. Therefore, all samples were scanned by means of micro-CT before and after PTA staining. In the datasets without staining, soft tissue structures were difficult to distinguish, as for example can be seen in Figure 1. Therefore, only the bony ossicles (malleus, incus and stapes) of the ME could be segmented confidently in the unstained datasets. After conversion into surface models, the two incudes of the datasets before and after staining were aligned based on a minimal surface distance algorithm, so that the difference in spatial position of the incus is almost zero between the datasets.

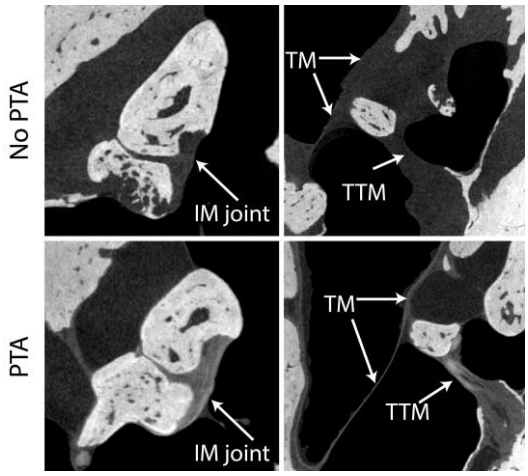

Figure 1. *Comparison of soft-tissue contrast on µCT images of the same temporal bone sample (sample 1) before and after PTA staining. Slices are in slightly different orientations because the sample was removed from the scanning stage between the scans. Also note the improved contrast between tissue and fluid that is in contact with the tissue in the PTA-stained images. IM joint: Incudomallear joint; TM: Tympanic membrane; TTM: Tensor tympani muscle.*

Then, using Amira® software tools, two 3D angles were determined, to quantify the angle change in the incudomallear joint (IMJ) and the incudostapedial joint (ISJ) respectively. First, the angle $\alpha = \widehat{ABC}$ was measured, in which *A* and *C* are the most inferior points of the malleus in the 'before' and 'after' dataset, respectively, and *B* the central point of articulation in the IMJ. The determination of point *B* is somewhat subjective, but careful attention was paid to choosing it consistently. Second, the angle $\beta = \widehat{DEF}$ was measured, in which *D* and *F* are points on the stapes footplate in the 'before' and 'after' dataset, respectively, and *E* the central point of articulation in the ISJ, which is easier to determine compared to point *B* due to the simpler shape of the ISJ. Points *D* and *F* are defined as the

outer point of the medial surface of the stapes footplate in the direction of maximal rotation between the 'before' and 'after' datasets. Figure 2 presents an example of the measurements of these angles in one sample. Furthermore, we observed the dominant axes and direction of rotation and categorized them into anatomical axes and directions, to ascertain whether these properties are consistent, regardless of the magnitude of the angles.

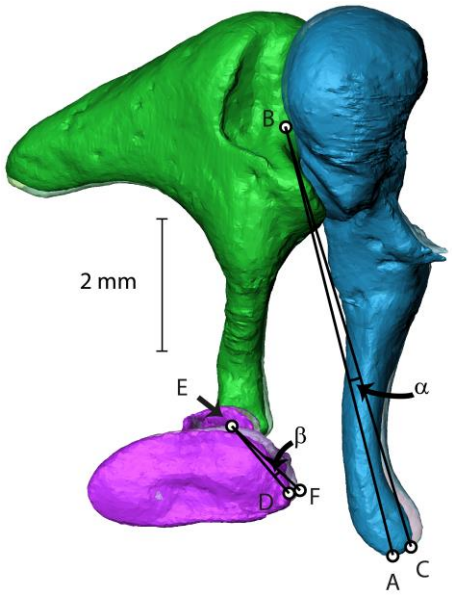

Figure 2. *Influence of PTA-staining on the ossicle configuration of sample 1. This figure is in isometric perspective for a better appreciation of distances. This sample showed overall the largest deformation of all samples. The opaque ossicles represent the dataset before staining and the transparent ossicles represent the dataset after staining. Points A, B and C define angle α and points D, E and F define angle β, as described in section 2.3.I, which represent the ossicular joint angle change between the datasets.*

Topic II: Middle Ear Ligaments

We aimed to identify the different ligaments in each ME sample and determine their prevalence, starting and attachment points and runway direction. Specific remarks on the individual ligaments were noted. The assessment of the presence of different ligaments was performed by interpreting the virtual 2D slices and by visualizing the data using a 3D rendering method in Amira®. This mode visualizes the CT image stack by assigning transparency to each voxel depending on its gray value. The thresholds for maximal and minimal transparency can be adjusted. This way, the often difficult-to-distinguish ligaments could be detected, identified and evaluated at the aforementioned criteria.

Topic III: Ossicle Parameters and Dimensions

The obtained data are perfectly suitable to evaluate multiple earlier studied parameters of the ME ossicles. For this purpose, a rigidly defined coordinate system needed to be chosen and applied consistently. The coordinate system chosen for this work is visualized in Figure 3. The origin is located at the most inferior point of the malleus (= the umbo). The *y*-axis runs superiorly, the *z*-axis medially and the *x*-axis posteriorly. Therefore, the coordinate system is either right-handed (for a right ear) or left-handed (for a left ear). The orientation of the *xy*-plane is determined to be parallel to the plane of the annular ligament.

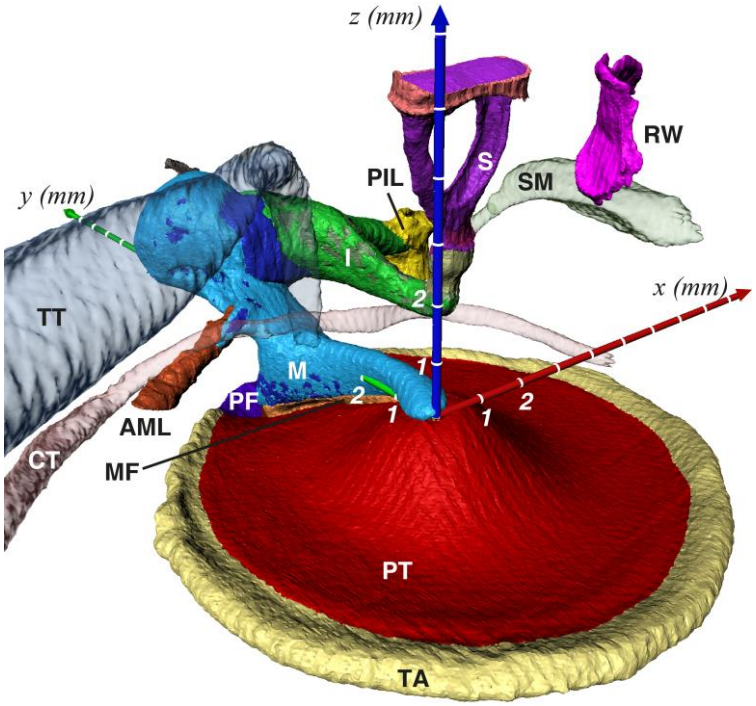

Figure 3. *Overview of the entire ME surface model of sample 2. Not all ligaments and mucosal folds are shown, for reasons of clarity. The abbreviations represent: PT: Pars tensa of the TM; PF: Pars flaccida of the TM; TA: Tympanic annulus; M: Malleus; I: Incus; S: Stapes; TT: Tensor tympani & tendon; SM: Stapedius muscle & tendon; MF: Manubrial fold; AML: anterior mallear ligament; PIL: posterior incudal ligament; CT: Chorda tympani; RW: Round window of the cochlea.*

Starting from the 3D surface models, created as explained in section 2.2, we determined the volumes of the ossicles and their intertrabecular spaces (defined below), as well as the ratio of intertrabecular space volumes to ossicle volumes; mechanical parameters such as the mass, the center of mass (COM), the principal moments of inertia (PMI) and the principal axes of rotation (PAR); and spatial dimensions such as those defining the ossicle lever arm ratio, but also other dimensions that are often mentioned in literature.

The ossicles are no solid bodies, but contain internal blood vessels (Kirikae, 1960) and cavities containing connective tissue, for example at the distal end of the long process of the incus (Karmody et al., 2009). From here on, we will refer to both these inhomogeneities as the “intertrabecular spaces” of the ossicles. The influence of these lower-density spaces on mechanical parameters such as COM, PMIs and PARs has not been quantitatively assessed yet. Therefore, we have separated the bony parts from the non-bony intertrabecular spaces during segmentation, and have calculated all mechanical parameters for two different cases:

1. Homogeneous ossicles: the mass density for intertrabecular spaces was equal to bone and the homogeneous ossicle densities were based on literature values of total ossicle densities.
2. Inhomogeneous ossicles: the intertrabecular spaces were assigned a lower mass density, based on literature values for soft tissue and blood, while the mass density of the bone was increased to make the total mass of the ossicles equal to case 1.

To test for significant differences in results between density cases 1 and 2, a non-parametric repeated measures test, the Wilcoxon signed rank test, was applied. Statistical significance is assumed when $p < 0.05$.

For our calculations, average mass density values of 2.31 g/ml and 2.14 g/ml for the malleus and the incus bone, including intertrabecular spaces, respectively were taken from Sim and Puria (2008). For the stapes, the average mass density of 2.20 g/ml was taken from Zhao et al. (2009). The intertrabecular spaces were assigned a density value of 1.06 g/ml (Harley et al., 1977; Cutnell and Johnson, 1999; Joseph et al., 1999; Alexander, 2003). For a discussion and motivation of these values, we refer to the 'Discussion' section.

Calculation of the mechanical parameters – In order to calculate different mechanical parameters, the surface models of the ossicles were converted to volume models, constructed of tetrahedral volume elements using a native Amira® algorithm. This allowed the assignment of different mass density values to the different structures. The coordinates of the tetrahedral meshes were imported in MATLAB[1], where subsequent calculations resulted in values for the following parameters:

- volume and mass of the bony ossicle and the intertrabecular spaces,
- COMs of the entire ossicles, comprising bone and intertrabecular spaces,
- PMIs of the entire ossicles, absolute and relative to individual mass density, and
- PARs of the entire ossicles.

The inertia parameters of each structure were determined through the following steps

- Translation of the origin to the COM of the studied structure.
- Calculation of the individual moments of inertia $I_{x_i x_i,k}$ and products of inertia $I_{x_i x_j k}$ of all elements through the following equations:

$$I_{x_i x_i,k} = m_k . d_{x_i,k}^2 , \quad (1)$$

$$I_{x_i x_j,k} = m_k . d_{x_i,k} . d_{x_j,k} , \quad (2)$$

  where m_k denotes the mass of element k and $d_{x_i,k}$ the perpendicular distance of element k to axis $x_i = x, y$ or z.

- Construction of the inertia matrix $\left[I_{x_i x_j}\right] = \left[\sum_k I_{x_i x_j,k}\right]$.
- Calculation of the eigenvalues and eigenvectors of the inertia matrix by diagonalization of the matrix. The PMIs are the eigenvalues, the PARs are the eigenvectors.

In addition to the separate ossicles, the algorithms were performed on the incudomallear complex (IMC), including the malleus and the incus, their intertrabecular spaces and the IMJ tissue. The IMJ tissue was assigned the same density value as the intertrabecular spaces, as it mainly consists of collagen, cartilage and synovial fluids. Besides the calculation of the PMIs, the following parameters were calculated as well:

[1] MATLAB Release 2012b, The MathWorks, Inc., Natick, Massachusetts, United States.

- I_{tot}: the total moment of inertia of the IMC for rotation around its anatomical rotation axis (which is classically defined as the axis connecting the tips of the anterior process of the malleus and the short process of the incus); calculated numerically;
- $I_{\mathrm{AnAx-COM}}$: the moment of inertia of a point particle with mass m_{IMC} and located at the COM of the IMC, for rotation around the anatomical axis; calculated using $I_{\mathrm{AnAx-COM}} = m_{\mathrm{IMC}}.d^2_{\mathrm{AnAx-COM}}$, with $d_{\mathrm{AnAx-COM}}$ the perpendicular distance from the COM to the anatomical axis.

Finally, the ratio $r_{\mathrm{eff}} = I_{\mathrm{AnAx-COM}}/I_{\mathrm{tot}}$ and the relative frequency shift $\Delta f_n = \sqrt{\frac{I_{\mathrm{tot}} - I_{\mathrm{AnAx-COM}}}{I_{\mathrm{tot}}}} - 1$ were calculated. The interpretations of these values are elaborated in the Discussion of the paper. The intention of these calculations was to determine the degree of efficiency loss and natural frequency alteration due to misalignment of the COM of the IMC away from the anatomical axis (Fleischer, 1978).

Ossicle dimensions – Three groups of ossicle dimension measurements were performed. For a visual indication of all measurement locations, see Figure 4.

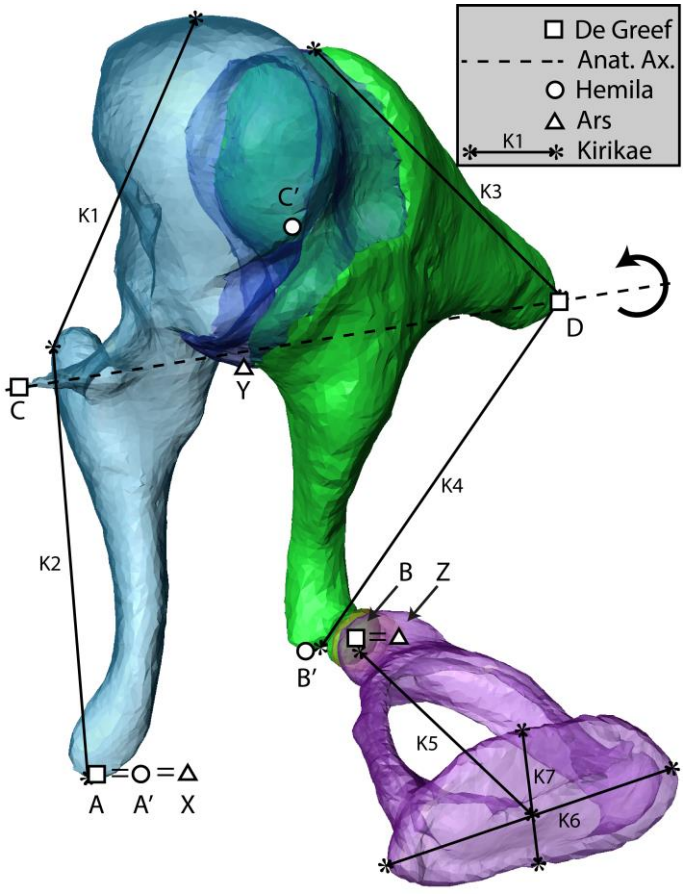

Figure 4. *Illustration of all measured ossicle dimensions. For detailed descriptions, see text section 2.3.III. Data from sample 2.*

- First, the classic lever arm ratio of the IMC was assessed. To this end, the coordinates of four anatomical points were measured: the inferior tip of the malleus (A), the middle point of the distal plate of the lenticular process of the incus (B), the tip of the anterior mallear process

(C) and the tip of the short process of the incus (D). Points C and D define the classic anatomical axis of rotation of the IMC, while points A and B represent the end points of the ossicles when they are considered as lever arms. These points are indicated by squares and the anatomical axis by a dashed line in Figure 4. Then the perpendicular distances from points A ($d_{1,ax}$) and B ($d_{2,ax}$) to the anatomical axis were calculated using the following formula (for point A):

$$d = \frac{|(\boldsymbol{A} - \boldsymbol{C}) \times (\boldsymbol{A} - \boldsymbol{D})|}{|\boldsymbol{D} - \boldsymbol{C}|}, \quad (3)$$

where the bold symbols represent the vector notation of the coordinates of the points. The formula for the distance from point B to the axis was analogous.

In order to compare this method to the suggested method in (Hemila et al., 1995), the following measurements were performed as well:

- $d_{1,IMJ}$: the distance from the inferior tip of the malleus (A') to the center point of the IMJ (C');
- $d_{2,IMJ}$: the distance from the inferior tip of the incus (B') to the same IMJ point (C').

These points are represented by circles in Figure 4.

- Secondly, multiple relevant ossicle dimension measurements as defined by Kirikae (1960) have been repeated on the new data:
  - Malleus: the length of the neck and the head (K1) and the length of the manubrium (K2);
  - Incus: the short process length (K3) and the length from the tip of the short process to the tip of the long process (K4);
  - Stapes: its height (K5) and the long (K6) and short diameter (K7) of the stapes footplate.

  These distances are indicated by solid lines ending in asterisks (*) in Figure 4.
- Thirdly, three ossicle lengths that are relevant according to Ars (1977) were reproduced: The distance from the manubrium tip (point X) to the inferior point of the IMJ (point Y); from the middle of the lenticular process of the incus (point Z) to point Y; and from point X to point Z. These points are denoted by triangles in Figure 4.

Topic IV: Morphology of the Distal Incus

The distal part of the incus includes three distinct bony components that are surrounded by soft tissue: 1. the long process of the incus that runs inferiorly from the body of the incus; 2. a thin lateral-medial bony connection (referred to as pedicle); and 3. an oval shaped disk perpendicular to the lateral-medial direction. The long lasting confusion regarding these features, as well as their relevance, will be discussed in section 4.2. During the segmentation we have distinguished between the bony core of the incus and the surrounding soft tissue, including collagen, joint tissue and blood vessels. As consistent as possible, the anterior-posterior width of the bony pedicle at its narrowest and widest point, and the superior-inferior thickness of the pedicle have been measured in each sample. These measurements were performed on the 3D surface models.

Topic V: TM and stapes footplate Areas

Using the high-resolution 3D surface models that were constructed in this work, it was possible to determine both the area of the lateral surface of the TM's pars tensa and the of the medial surface of

the stapes footplate (SFP) with a good accuracy. To assess the influence of different possible approaches, the areas were calculated in three different ways:

1. The ellipse approximation: The short and long diameters (a and b) of both TM and SFP were measured in Amira® and the subsequent ellipse surface was calculated through $S_{\text{ell}} = \pi ab/4$.
2. 2D projection: The surface area of the conical TM is approximated by the surface area of the 2D projection of the lateral TM surface onto the plane that is defined by the tympanic annulus. The slightly irregular medial surface of the SFP was projected onto the plane defined by the annular ligament. The areas were calculated through a pixel counting technique in MATLAB.
3. 3D surface: The real surface area was calculated, taking into account the curvature and irregularities of the surfaces. This was performed using a native algorithm of Amira®, based on the triangulated surface models.

All measurements of the TM surface area were performed on the pars tensa only, as the pars flaccida is believed to have little to no contribution to sound collection (Rosowski, 1994).

Topic VI: Thickness of Different Structures

The segmented voxel data of the TM was subjected to the 'Shortest distance' thickness algorithm as described in Van der Jeught et al. (2013), and a possible correlation between the resulting mean thickness of the TM and the inferior-superior length of the TM was calculated, as suggested in Van der Jeught et al. (2013) as well.

For three other structures we could determine relevant thickness values as well: the ossicle joint gaps, the stapedial annular ligament and the round window of the cochlea. The thickness of the joints corresponds to the gap between the ossicles, while the SAL thickness corresponds to the gap between the SFP and the cochlea bone. These three structures, however, feature more irregular shapes than the TM and are therefore unsuited for application of any of the automated algorithms of Van der Jeught et al. (2013). A native thickness calculation of Amira® was applied and the minimal thickness, maximal thickness and the locations of both were manually measured on the surface models.

3. Results

Figure 1 illustrates the difference in soft-tissue contrast on µCT images of the same temporal bone sample between pre- and post-stained samples for different ME structures. Figure 3 provides an overview of the entire ME surface model for one of our samples. For clarity reasons, not all ligaments are included in the figure and some structures are depicted transparently. In general, to summarize results for all six samples, we provide the average and corrected standard deviation as statistical parameters. The uncertainty for length measurements on the data is equal to the voxel size of 20 µm. If the standard deviation of a set of measurements is smaller than this individual measurement error, we mention the individual error as uncertainty intervals in the text.

3.1 Topic I: Effect of PTA on Ossicle Configuration

Table 2 presents the results of the manual measurement of the incudomallear joint (IMJ) angle change ($\alpha = \widehat{ABC}$) and incudostapedial joint (ISJ) angle change ($\beta = \widehat{DEF}$), as explained in section

2.3.I, as well as their categorized axis of rotation and the direction of positive rotation. For both angles α and β, only the magnitude of the angles are reported, while their sign is communicated through the direction of rotation. The measurement error for every angle measurement was estimated to be 0.2˚, being the largest difference between multiple independent repetitions of the same measurement. It is apparent that for both joints, neither a consistent axis nor direction of rotation is found, with only a slight favor for rotation towards inferior around the anterior-posterior axis for the ISJ. The mean rotation magnitude (independent from the axis or direction) for the IMJ is $(1{,}10 \pm 0{,}67)^{\circ}$ and for the ISJ is $(1{,}3 \pm 1{,}0)^{\circ}$. Furthermore, observed angle changes are never larger than 3,0°. Figure 2 gives a visual impression of the magnitude of the ossicle rotation. The presented model is sample 1, for which the angle changes in the IMJ and the ISJ are respectively 2.1° and 1.9°, two of the three largest angle changes in our dataset. For this figure, like for the angle measurements, the incudes of both datasets are aligned as well as possible.

Table 2. *Influence of PTA staining on ossicle configuration. α and β represent the angle changes in the IMJ and ISJ, respectively, between micro-CT measurements before and after staining and have measurement errors of 0,2˚. For easy interpretation, the axes and direction of rotation are categorized into anatomical axes and directions.*

	Incudomallear joint			**Incudostapedial joint**		
	α (°) *	**axis**	**direction**	**β (°) ***	**axis**	**direction**
Sample1	2,1	lat-med	ant	1,9	sup-inf	ant
Sample2	0,8	lat-med	post	0,0	-	-
Sample3	1,8	lat-med	ant	1,3	ant-post	inf
Sample4	0,5	ant-post	lat	0,6	ant-post	inf
Sample5	0,7	ant-post	lat	1,1	ant-post	inf
Sample6	0,7	ant-post	lat	3,0	ant-post	inf
Mean (°)	1,10			1,3		
St. dev. (°)	0,67			1,0		

* ± 0,2°

3.2 Topic II: Middle Ear Ligaments

General observations

One general observation is the difficulty to identify some of the ligaments, because all ligaments are embedded in and bordered by larger mucosal folds and strands that envelope all structures in the ME (Gulya and Schuknecht, 1995). Hence, multiple spaces in the ME are formed, such as Prussak's space, the interior incudal space, and the anterior and posterior pouches of von Troeltsch (Sanjay et al., 2012). Figure 5 provides an impression of the mucosal folds around the ossicles and their ligaments. We have identified structures as being ligaments only if they were clearly distinguishable and had a higher gray value on the CT slices than other soft tissue structures surrounding the ossicles. All other ambiguous strands and folds of tissue were identified as mucosa strands.

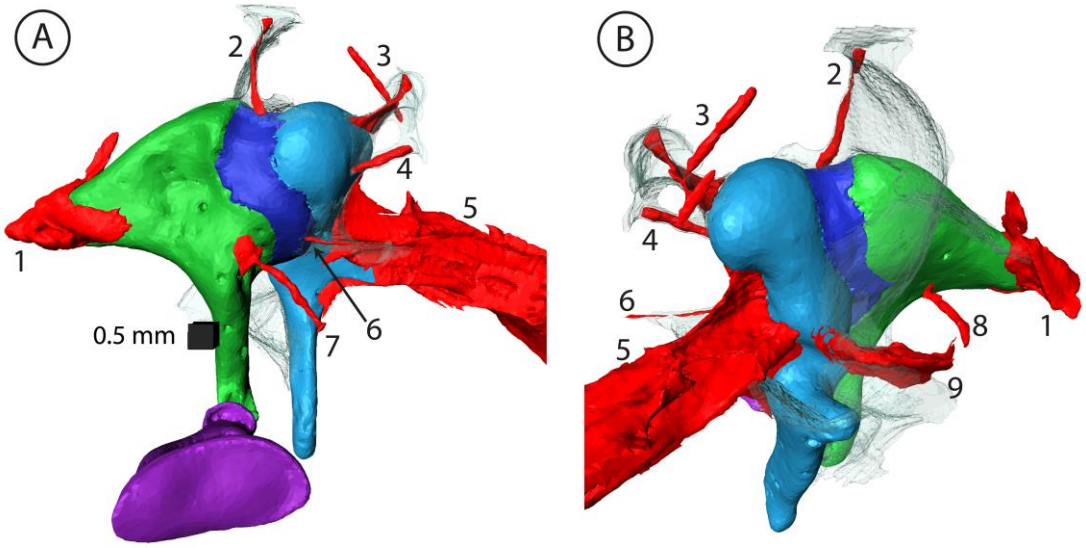

Figure 5. *Mucosal folds and strands surrounding the ME ossicles and ligaments in sample 4. A. Medial view. B. Latero-superior view. Structures identified as ligaments are red and opaque, mucosa is transparent. The AML is not shown to its full extent to limit the size of the figure. The numbered ligaments are (for abbreviations see table 1 or 3): 1. PIL; 2. P-SML ; 3. A-SML; 4. S-AML; 5. AML; 6. M-AML; 7. MIL; 8. LIL; 9. LML. Notice that, in this sample, both the P-SML and the S-AML attach to the IMJ, rather than to the malleus.*

Table 3 summarizes our findings for all observed ME ligaments, including their starting and attachment points, runway direction and ligament-specific remarks in the footnotes.

Sample 5 had remarkably many deviations from the other samples in terms of ligaments. Some floating bone shards were observed in the ME cavity, suggesting a fractural trauma in the temporal bone, which could explain the absence of some ligaments that were found in the other samples.

Observed irregularities for specific ligaments

The structure that has been named posterior mallear ligament (PML) was never confidently interpreted as a ligament, but rather as mucosal strands and folds. There was however consistency in its appearance (observed in all 6 samples) and we acknowledge probable confusion when observing this structure in surgical circumstances. The same remark of possible confusion is valid for the superior anterior mallear ligament (S-AML) (prevalence of 1/6).

Two ligaments had remarkable variation in attachment point to the ossicular chain: the posterior superior mallear ligament (P-SML) and the medial anterior mallear ligament (M-AML). Both ligaments attach to the malleus surface in some samples, blend with the capsule of the IMJ in others, and exhibit a combination in yet other samples. This could very well be another source of confusion in nomenclature between different authors. The P-SML could also be named the superior incudomallear ligament, similar for the M-AML, which could be identified as an anterior incudomallear ligament.

Two ligaments were only seen in one sample (not the same sample): the superior anterior mallear ligament (S-AML) and the superior stapedial ligament (SSL). For an impression of the SSL, see Figure 6.

Table 3. *Properties of all observed ligaments or mucosa structures that could be confused with ligaments.*

	Ligament	Abbrev.	Prevalence	Origin	Attachment	Direction	Remarks
Malleus	Anterior	AML	6/6 (100 %)	Ant. proc. and neck of the mall.	PTF wall	Ant	Very thick and long; Only partially attaches to the PTF wall and then runs through beyond our dataset limits.
	Medial anterior	M-AML	5/6 (83 %)	Ant. surface of mallear head and/or IMJ capsule; medially to AML	Mastoid bone	Ant-med(-inf)	Very thin; Can also originate from the IMJ capsule with partial or full attachment
	Superior anterior	S-AML	1/6 (17 %)	Ant. surface of mallear head; superior to AML	Cavity wall	Ant-sup	In literature also referred to as anterior suspensory mallear ligament (Gulya and Schuknecht, 1995; Mikhael, 2005)
	Lateral	LML	6/6 (100 %)	Neck of the malleus	Cavity wall	Lat-post	Sometimes connects to PML and/or CT at the point of attachment.
	Posterior	PML	6/6 (100 %)	Posterior side of manubrium	Cavity wall	Post	Difficult to distinguish between mucosa and ligament; Passes very closely to CT (laterally), often making contact to it.
	Anterior superior	A-SML	3/6 (50 %)	Sup-ant. surface of mallear head	Cavity wall	Ant-sup	Surrounded by mucosa.
	Posterior superior	P-SML	5/6 (83 %)	Sup-post-med. surface of mallear head and/or sup. IMJ cap	Cavity wall	Sup-post-med	Can also originate from the IMJ capsule with partial or full attachment; Could easily be confused with a IM ligament in some samples.
IMJ	Medial	MIML	1/6 (17 %)	Med. side of IMJ cap	Mastoid bone/cav. wall	Med	Splits into 3 branches, 2 running to the mastoid bone and 1 to the cavity wall
Incus	Posterior	PIL	6/6 (100 %)	Med. and lat. side of short process of the incus	Cavity wall	Med OR Lat	Consists of two distinct but connected portions: medial and lateral
	Medial	MIL	3/6 (50 %)	Med. side of the upper part of the long process of the incus	Cavity wall	Med OR Med-ant-sup	Very thin; One instance of a ligament starting on the short process of the incus.
	Lateral	LIL	5/6 (83 %)	Lat. side of the middle part of the long process of the incus	CT	Lat	Very short; One instance with two branches.
Stapes	Superior	SSL	1/6 (17 %)	Sup-ant. side of stapes head	Cochlea bone	Sup-ant	Very thin; at the opposite side of the stapedius muscle tendon (attached posteriorly to the stapes head)

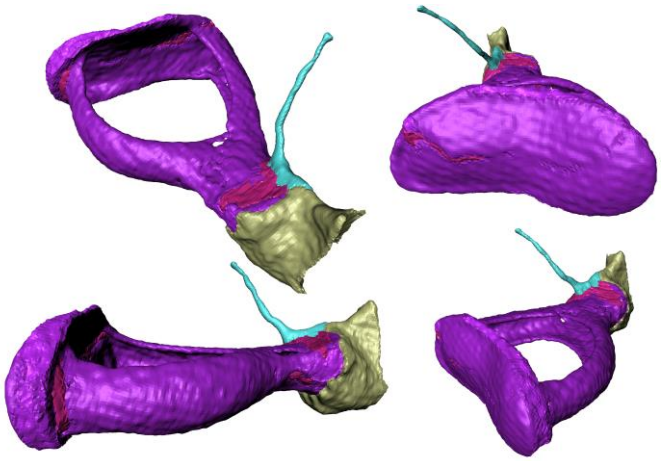

Figure 6. *Different views of the superior stapedial ligament (thin, light green structure) of sample 5.*

3.3 Topic III: Ossicle Parameters and Dimensions

Table 4 presents all results for the mechanical parameters of the ossicles using the inhomogeneous density case (case 2 as defined in section 2.3.III), while table 5 presents the principal moments of inertia (PMI) for the homogeneous density case (case 1). In both tables, statistical differences between cases 1 and 2 for the PMI are indicated by an asterisk (*). Although the differences between mean PMI are small compared to the standard deviation, the Wilcoxon signed-rank test, taking into account the "matched-pairs" nature of the datasets, reveals significant differences in 5 out of 9 cases. Figure 7 provides an impression of the intertrabecular spaces present in the ossicles.

The naming of the principal axes of rotation (PAR) directions in table 4 as ant-post (anterior-posterior), sup-inf (superior-inferior) and lat-med (lateral-medial) is an approximation and is no substitute for the vector notation, but facilitates interpretation of the results.

In table 6, the same information for the incudomallear complex is shown (also calculated using density case 2), added by the results of the calculations to assess the influence of the IMC's center of mass misalignment away from the anatomical rotation axis.

Table 7 shows the results from the measurements of the ossicular lever arm lengths, as well as the other ossicle dimension measurements as described in section 2.3.III and results from various other authors. The result for the lever arm ratio defined by the perpendicular distances from the umbo and the IS joint to the anatomical rotation axis induce a SPL increase of (2.28 ± 0.61) dB.

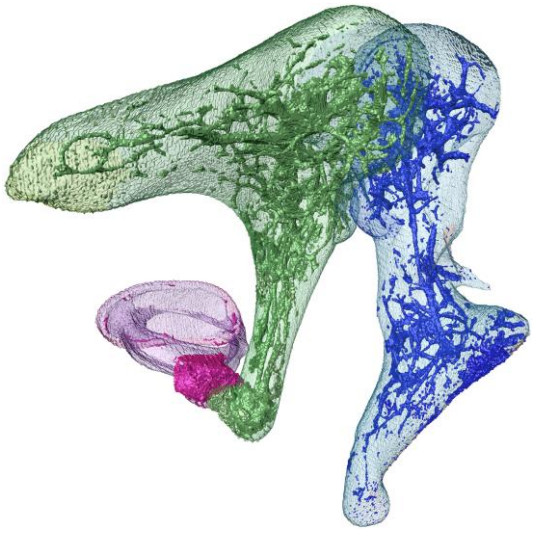

Figure 7. *Distribution of lower-density intertrabecular spaces inside the ossicles of sample 4. Bone is transparent. Fluid-filled or soft tissue-filled parts are opaque.*

Table 4. *Mechanical properties of the ossicle bones, using density case 2 (inhomogeneous ossicles). Density values are derived from literature (Sim and Puria, 2008; Zhao et al., 2009); all other values were calculated in this study. The coordinates are relative to the coordinate system described in section 2.3.III. For the principal moments of inertia, statistical differences between density cases 1 (homogeneous) and 2 (inhomogeneous), calculated using the Wilcoxon signed-rank test, are indicated by an asterisk (*). In the second lower row, approximated directions for the principal axes of rotations are given to facilitate interpretation.*

	Malleus			**Incus**			**Stapes**		
Density [10^3 kg/m^3]									
σ_{bone}	2,50			2,25			2,27		
σ_{soft}	1,06			1,06			1,06		
Volume [mm^3]									
V_{bone}	11,3 ± 1,4			12,28 ± 0,90			1,14 ± 0,11		
V_{soft}	0,57 ± 0,48			0,80 ± 0,42			0,105 ± 0,050		
V_{tot}	11,9 ± 1,4			13,1 ± 1,1			1,24 ± 0,13		
V_{soft}/V_{tot}	(4,8 ± 4,1) %			(6,0 ± 2,9) %			(8,4 ± 3,6) %		
Mass [mg]									
m_{bone}	26,9 ± 3,2			27,1 ± 2,1			2,62 ± 0,26		
m_{soft}	0,60 ± 0,51			0,85 ± 0,44			0,110 ± 0,050		
m_{tot}	27,5 ± 3,2			28,0 ± 2,4			2,73 ± 0,28		
m_{soft}/m_{tot}	(2,2 ± 1,9) %			(3,0 ± 1,4) %			(4,0 ± 1,7) %		
Center of mass [mm]									
x	-0,18 ± 0,19			1,95 ± 0,24			1,63 ± 0,21		
y	5,33 ± 0,23			5,89 ± 0,49			1,27 ± 0,41		
z	0,47 ± 0,42			0,87 ± 0,31			3,38 ± 0,40		
Principal moments of inertia									
I_1 [mg.mm^2]	15,0 ± 3,4 *			31,7 ± 5,4 *			1,88 ± 0,27 *		
I_2 [mg.mm^2]	97 ± 21			49,0 ± 6,3			3,98 ± 0,48 *		
I_3 [mg.mm^2]	102 ± 23			72,1 ± 7,1			5,38 ± 0,70 *		
I_1/I_3 []	(15,0 ± 2,3) %			(43,8 ± 5,1) %			(35,0 ± 2,0) %		
$I_2/_3$ []	(95,2 ± 1,2) %			(68,0 ± 5,3) %			(74,0 ± 1,0) %		
I_1/σ [mm^5]	6,5 ± 1,5			14,8 ± 2,5			0,86 ± 0,12		
I_2/σ [mm^5]	41,8 ± 9,0			22,9 ± 3,0			1,81 ± 0,22		
I_3/σ [mm^5]	44,0 ± 9,9			33,7 ± 3,3			2,45 ± 0,32		
Principal axes of rotation									
	Ax_1	**Ax_2**	**Ax_3**	**Ax_1**	**Ax_2**	**Ax_3**	**Ax_1**	**Ax_2**	**Ax_3**
x [mm]	-0,10	0,14	-0,98	0,11	0,97	0,09	-0,08	0,99	-0,05
y [mm]	0,93	-0,33	-0,14	0,98	-0,11	0,03	-0,17	0,03	0,98
z [mm]	0,34	0,93	0,10	-0,04	-0,09	0,99	0,98	0,09	0,17
Approx. dir.	**sup-inf**	**lat-med**	**ant-post**	**sup-inf**	**ant-post**	**lat-med**	**lat-med**	**ant-post**	**sup-inf**
MOI ratio	**15%**	**95%**	**100%**	**44%**	**68%**	**100%**	**35%**	**74%**	**100%**

*: $p < 0,05$ for comparison between density cases 1 (homogeneous ossicles) and 2 (inhomogeneous ossicles)

Table 5. *PMI results for the ossicles for density case 1 (homogeneous ossicles). Statistical differences between density cases 1 and 2 (inhomogeneous ossicles), calculated using the Wilcoxon signed-rank test, are indicated by an asterisk (*).*

	Malleus	Incus	Stapes
I_1 [mg.mm²]	14,9 ± 3,4 *	31,1 ± 5,1 *	1,82 ± 0,26 *
I_2 [mg.mm²]	95 ± 20	50,7 ± 6,9	4,13 ± 0,54 *
I_3 [mg.mm²]	100 ± 22	73,3 ± 8,3	5,49 ± 0,72 *

*: p < 0,05 for comparison between density cases 1 (homogeneous ossicles) and 2 (inhomogeneous ossicles)

Table 6. *Mechanical properties of the incudomallear complex, using lower density values for the intertrabecular spaces and the IMJ. Density values are derived from literature (Sim and Puria, 2008; Zhao et al., 2009); all other values are derived from our new data. All coordinates are relative to the coordinate system described in section 2.3.III and depicted in figure 3. In the second lower row, approximated directions for the principal axes of rotations are given to facilitate interpretation.*

Density [10³ kg/m³]	
$\sigma_{malleus}$	2,50
σ_{incus}	2,25
σ_{soft}	1,06
Volume [mm³]	
$V_{malleus}$	11,3 ± 1,4
V_{incus}	12,28 ± 0,91
V_{joint}	1,68 ± 0,29
V_{mall_can}	0,58 ± 0,46
V_{inc_can}	0,80 ± 0,40
V_{tot}	26,7 ± 2,4
V_{soft}/V_{bone} []	11,4 % ± 3,4 %
Mass [mg]	
$m_{malleus}$	26,9 ± 3,2
m_{incus}	27,2 ± 2,1
m_{joint}	1,78 ± 0,31
m_{mall_can}	0,62 ± 0,49
m_{inc_can}	0,85 ± 0,42
m_{tot}	57,3 ± 5,3
m_{soft}/m_{tot} []	5,6 % ± 1,7 %
Center of mass [mm]	
x	0,89 ± 0,21
y	5,63 ± 0,36
z	0,68 ± 0,37

Principal moments of inertia			
I_1 [mg.mm²]	114 ± 10		
I_2 [mg.mm²]	163 ± 32		
I_3 [mg.mm²]	237 ± 32		
I_1/I_3 []	0,485 ± 0,039		
$I_{2/3}$ []	0,682 ± 0,057		
I_1/σ [mm⁵]	53,2 ± 4,7		
I_2/σ [mm⁵]	76 ± 15		
I_3/σ [mm⁵]	110 ± 15		
Principal axes of rotation			
	Ax_1	**Ax_2**	**Ax_3**
x [mm]	0,29	0,95	-0,04
y [mm]	0,92	-0,28	-0,24
z [mm]	0,24	-0,03	0,97
Approx. direction	**sup-inf**	**ant-post**	**lat-med**
MOI ratio	**49%**	**68%**	**100%**
COM misalignment effect			
COM-AnAx [mm]	1,31 ± 0,19		
I_{AnAx_COM} [mg.mm²]	99 ± 28		
I_{tot} [mg.mm²]	265 ± 48		
$r_{eff} = I_{AnAx\_COM}/I_{tot}$	(37,1 ± 6,8) %		
Δf_n	(-20,8 ± 4,3) %		

Table 7. *Ossicle dimensions from our data and from various published sources. A dash (-) between two values denotes the range of values, rather than an uncertainty interval. Otherwise, a sole dash represents absent data. An asterisk (*) indicates data that does not overlap our data. References: (Kirikae, 1960; Ars, 1977; Anson and Donaldson, 1981; Hemila et al., 1995; Gan et al., 2002; Unur et al., 2002; Sim et al., 2013; Todd and Creighton, 2013; Quam et al., 2014).*

Dimension	Fig. 3 mark	De Greef	Kir 60	Hem 95	Ars 78	Ans 81	Unur 02	Gan 02	Todd 13	Sim 13	Quam 14
$d_{1,ax}$ [mm]	A - AnAx	4,47 ± 0,30	-	-	-	-	-	-	-	-	-
$d_{2,ax}$ [mm]	B - AnAx	3,45 ± 0,15	-	-	-	-	-	-	-	-	-
$d_{1,ax}/d_{2,ax}$ []	/	1,30 ± 0,11	-	-	-	-	-	-	-	-	-
$d_{1,IMJ}$ [mm]	A' - C'	6,28 ± 0,36	-	6,24	-	-	-	-	-	-	-
$d_{2,IMJ}$ [mm]	B' - C'	4,83 ± 0,14	-	4,46	-	-	-	-	-	-	-
$d_{1,IMJ}/d_{2,IMJ}$ []	/	1,30 ± 0,10	-	1,40	-	-	-	-	-	-	-
Malleus head + neck [mm]	K1	4,74 ± 0,29	5,0 ± 0,1	-	-	-	4,85 ± 0,29	-	4,9 ± 0,3	-	-
Malleus manubrium [mm]	K2	4,98 ± 0,39	4,51 ± 0,08*	-	-	4,33 - 5,67	4,70 ± 0,45	4,20*	4,8 ± 0,4	-	4,94 ± 0,31
Incus short proc length [mm]	K3	5,35 ± 0,21	4,81 ± 0,07*	-	-	-	4,88 ± 0,47	4,49*	5,0 ± 0,3	-	5,07 ± 0,37
Incus short to long proc [mm]	K4	5,73 ± 0,16	5,99 ± 0,08*	-	-	-	6,12 ± 0,43	-	5,9 ± 0,4	-	-
Stapes height [mm]	K5	3,37 ± 0,14	3,29 ± 0,15	-	-	-	3,22 ± 0,31	2,87*	-	3,28 ± 0,210	3,44 ± 0,20
SFP long diameter [mm]	K6	2,73 ± 0,10	2,96 ± 0,15	2,99*	-	2,64 - 3,36	2,57 ± 0,33	2,5*	-	2,81 ± 0,158	2,94 ± 0,14
SFP short diameter [mm]	K7	1,306 ± 0,086	1,33 ± 0,11	1,27	-	1,08 - 1,66	1,29 ± 0,22	1,38	-	1,27 ± 0,109	1,39 ± 0,10
Ars XY [mm]	X - Y	4,68 ± 0,34	4,65 ± 0,09	-	4,5 ± 0,5	-	-	-	-	-	-
Ars YZ [mm]	Y - Z	3,19 ± 0,21	-	-	3,1 ± 0,5	-	-	-	-	-	-
Ars XZ [mm]	A - Z	2,81 ± 0,48	-	-	2,5 ± 0,5	-	-	-	-	-	-

* Ranges not overlapping our data

3.4 Topic IV: Morphology of the Distal Incus

Figure 8 shows an example of minimum and maximum width measurements of the pedicle width on sample 6.The results of the width (w_{min} and w_{max}) and thickness (d) measurements on the pedicles on all measurements are shown in table 8, as well as a description of their shapes. Both the pedicle's dimensions and shapes feature large inter-individual differences. Besides inconsistent, pedicle shapes are very irregular as well. To give an impression of the irregularity and inconsistency, Figure 9 presents superior views of the pedicles in all samples.

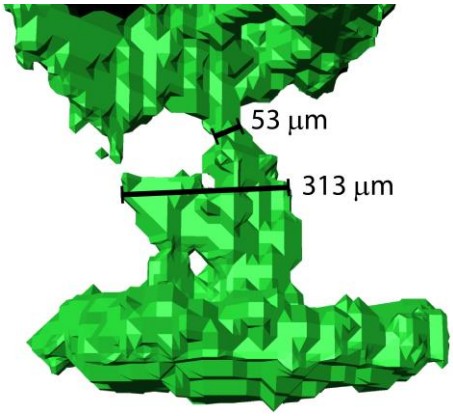

Figure 8. *Example of a measurement of the minimal and maximal width of the bony pedicle at the lenticular process of the incus in sample 6. The measurement unit is µm. The precision of the measurement is obviously not 0.01 µm but 20 µm.*

There was in every sample, however, at least one uninterrupted bony connection between the long process of the incus and the lenticular process, even if only a few pixels wide or thick. In none of the samples, the bony pedicle was completely interrupted. Based on their observed high X-ray absorption, the pedicles all consist of either bone or dense calcified cartilage.

Table 8. *Properties of the bony pedicle of incudal the lenticular process in all samples. We measured the minimal (w_{min}) and maximal width (w_{max}) (both in anterior-posterior direction), and the thickness (d) (in superior-inferior direction). Furthermore, a qualitative description of the appearance of the bony connection is provided.*

Sample	w_{min} ± 20 (µm)	w_{max} ± 20 (µm)	d ± 20 (µm)	Description of appearance
1	246	338	53	Single connection; multiple holes
2	81	387	55	Single connection; irregular, twisted shape
3	260	319	62	Single connection; 1 large hole
4	351	395	50	Single connection; 1 small hole
5	461	559	48	Three equivalent parts
6	53	313	55	1 true connection; 1 very thin/interrupted
Mean	**242**	**385**	**53,8**	
St. Dev.	**156**	**92**	**4,8**	

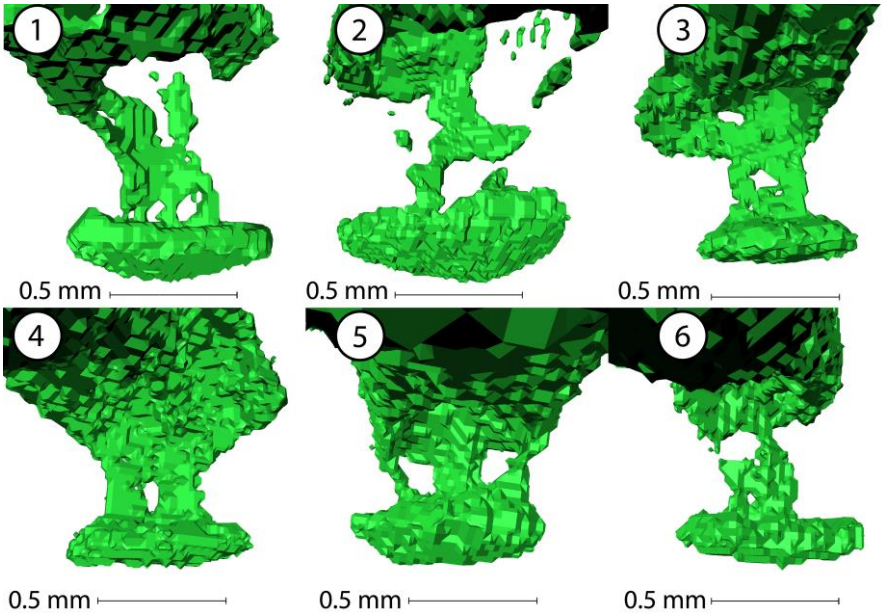

Figure 9. *Superior views of the incudal lenticular processes of all samples. All scale bars represent 0.5 mm. The views are in perspective but the scale bars are always in the plane of the pedicle of the lenticular process.*

3.5 Topic V: TM and stapes footplate Areas

The results of all operations described in section 2.3.V are listed in table 9. The uncertainty values for the surface areas and ratio obtained using the ellipse approximation originate from the individual error on the length measurements, which is chosen equal to the voxel size, and are calculated through error propagation. These values are slightly different for each sample but equal after rounding.

Table 9. *Surface areas of both the pars tensa of the TM and the SFP, using three different approaches, as well as the derived hydraulic area ratio for all samples and methods.*

	TM surface area (mm^2)			SFP surface area (mm^2)				Hydraulic Ratio		
Sample	Ellipse*	2D Proj	3D Surf	Ellipse**	2D Proj	3D Surf		Ellipse***	2D Proj	3D Surf
1	64,12	66,0	71,4	2,87	3,15	3,37		22,3	21,0	21,2
2	64,45	65,9	69,8	2,84	3,08	3,21		22,7	21,4	21,7
3	55,64	58,1	63,0	2,69	2,85	3,06		20,7	20,3	20,6
4	57,94	60,0	64,8	3,14	3,29	3,55		18,4	18,2	18,3
5	45,22	47,3	56,0	2,59	3,04	3,31		17,5	15,6	16,9
6	58,20	59,4	68,5	2,67	2,84	3,06		21,8	20,9	22,4
<S>	**57,6**	**59,4**	**65,6**	**2,80**	**3,04**	**3,26**	**<R>**	**20,6**	**19,6**	**20,2**
σ_S	**7,0**	**6,9**	**5,6**	**0,20**	**0,17**	**0,19**	**σ_R**	**2,1**	**2,3**	**2,1**

* ± 0,06 mm2

** ± 0,02 mm2

*** ± 0,4

The result for the hydraulic ratio induce a SPL increase of (26.26 ± 0.91) dB, (25.83 ± 1.00) dB and (26.10 ± 0.71) dB, for the ellipse, 2D projection and 3D surface methods respectively.

When compared one-to-one, all mutual differences between the three different surface area estimation methods are statistically significant ($p < 0.05$; tested using the Wilcoxon signed-rank test) for the TM surface area, stapes footplate (SFP) surface area and hydraulic ratio. The sole exception is the difference between the hydraulic ratio calculated through either the Ellipse method (for both TM and SFP) or the 3D surface method ($p = 0.2188$).

Conversion factors to convert the surface area, obtained by means of the ellipse (S_{ell}) or 3D surface ($S_{3\text{D}}$) method, to the 2D projected surface area ($S_{2\text{D}}$) were calculated:

- TM
  - $S_{2\text{D}}/S_{\text{ell}} = (103.3 \pm 1.0)\%$
  - $S_{2\text{D}}/S_{3\text{D}} = (90.4 \pm 4.0)\%$
- SFP
  - $S_{2\text{D}}/S_{\text{ell}} = (108.8 \pm 4.6)\%$
  - $S_{2\text{D}}/S_{3\text{D}} = (93.3 \pm 1.4)\%$

These numbers allow authors with different surface data to easily compare or convert their numbers to projected surface areas.

3.6 Topic VI: Thicknesses of Different Structures

Application of the 'shortest distance' algorithm on the current TM datasets resulted in six thickness maps, one of which is shown in Figure 10. The mean thickness $\langle d \rangle$ over the entire pars tensa, excluding the tympanic annulus and the part of the TM that is connected to the manubrium (similar to Van der Jeught et al. (2013)) was calculated for every sample and was on average (81 ± 18) µm, ranging from (59 ± 35) µm to (106 ± 35) µm. The thickness distribution of the different samples did not suggest a consistent local thickening of the membrane in certain quadrants, and the correlation between the mean TM thickness $\langle d \rangle$ and the inferior-superior length $l_{\text{inf-sup}}$ of the TM was insignificant at $R^2 = 0.0037$, both in contrast to Van der Jeught et al. (2013). Table 10 presents the individual values of these parameters.

To study the thickness of the IMJ, a distinction was made between the consistent excessively thick bulge at the medio-superior part of the joint and the remaining part of the IMJ. For this remaining part, minimum and maximum thicknesses were located and measured. For the ISJ, minimum and maximum thicknesses were recorded as well. The same approach was used for the stapedial annular ligament (SAL) and the round window of the cochlea (RW). All results are given in table 11 (IMJ and ISJ) and 12 (SAL and RW). In sample 6, the RW was ruptured; hence no data are available for said sample. An impression of the thickness datasets of these four structures is presented in Figure 11.

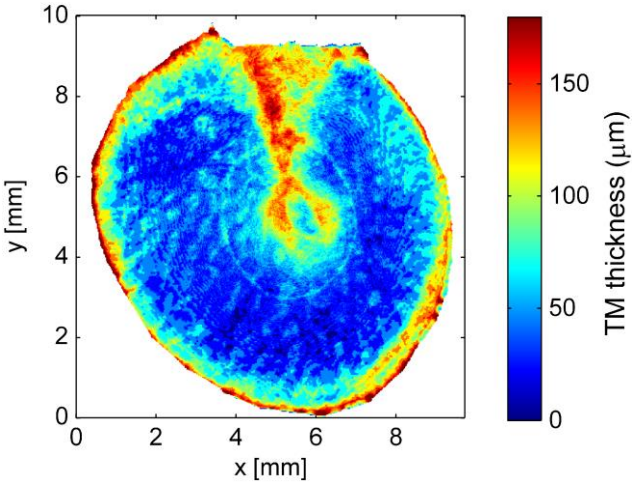

Figure 10. *Thickness distribution of the TM of sample 2. Thickness values were calculated using the 'Shortest distance' algorithm from Van der Jeught et al. (2013).*

Table 10. *Average thickness* $\langle d \rangle$ *and inferior-superior length of the pars tensa of the TM in all samples. The standard deviation for each individual samples represents the variation of thickness over the entire pars tensa surface.*

Sample	<d> (µm)	σ_d (µm)	$l_{inf\text{-}sup}$ (mm) *
1	59	35	9,09
2	93	32	9,34
3	91	31	8,15
4	106	35	8,42
5	66	29	8,00
6	73	39	8,75
Mean	81		8,62
StDev	18		0,53

* ± 0,02 mm

Table 11. *Minimal and maximal local thicknesses d of the IMJ and ISJ, as well as the locations of the minimal and maximal thicknesses for all samples. Furthermore, the thickness of the excessive bulge of the IMJ, that is located medio-superiorly, is presented.*

	Incudomallear joint						Incudostapedial joint			
	Miminum		Maximum		Bulge		Miminum		Maximum	
sample	d (μm) *	Loc	d (μm) *	Loc	d (μm) *	Loc	d (μm) *	Loc	d (μm) *	Loc
1	30	lat	230	inf	1000	med-sup	75	multi	145	post
2	30	lat-sup	240	multi	1150	med-sup	90	sup	190	post
3	30	lat	240	multi	900	med-sup	80	ant	120	post-inf
4	30	lat-sup	250	sup	950	med-sup	75	multi	130	sup
5	40	multi	230	mid	950	med-sup	80	ant-inf	240	post-sup
6	50	lat	220	mid	950	med-sup	70	multi	150	post-sup
Mean	35,0		235		983		78,3		163	
StDev	8,4		10		88		6,8		45	

* ± 20 mm

Table 12. *Minimal and maximal local thicknesses d of the SAL and RW, as well as the locations of the minimal and maximal thicknesses for all samples.*

	Stapedial annular ligament				Round window of the cochlea			
	Miminum		Maximum		Miminum		Maximum	
Sample	d (μm) *	Loc	d (μm) *	Loc	d (μm) *	Loc	d (μm) *	Loc
1	0	multi	340	ant	45	sup-lat	250	med
2	13	multi	280	ant-inf	35	lat	235	lat-sup
3	0	multi	210	ant-inf	75	mid	260	mid
4	22	multi	330	ant	60	ant-inf	170	ant-inf
5	0	multi	230	ant-inf	60	multi	190	med
6	0	multi	350	ant	N/A	N/A	N/A	N/A
Mean	5,8		290		55		221	
StDev	9,5		60		15		39	

* ± 20 mm

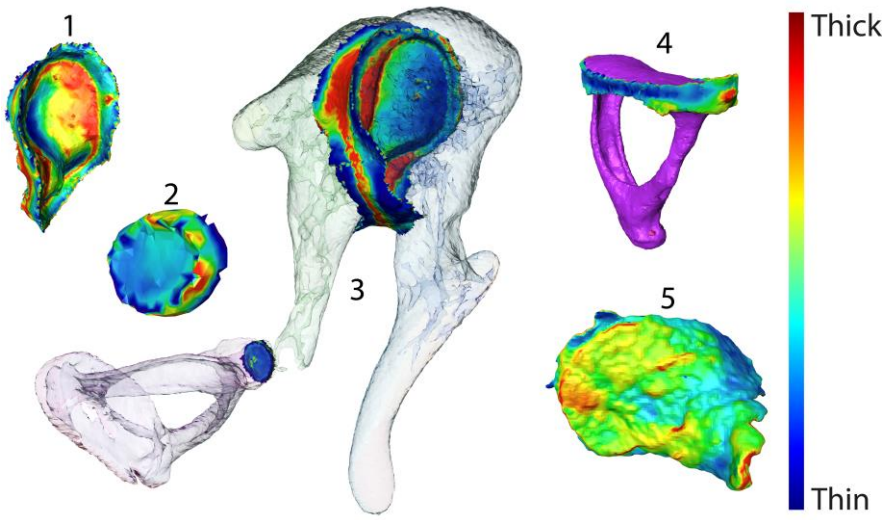

Figure 11. *Examples of thickness distributions of 1. IMJ; 2. ISJ; 4. SAL attached to the stapes; and 5. RW of the cochlea. Subfigure 3 presents IMJ and ISJ data inserted in the entire ossicular chain with transparent ossicles. The different structures are not in their correct relative spatial positions. The color map limits are different for different structures; all extreme values are listed in tables 11 and 12. Data for 1,2 and 4 are from sample 4. Data for 3 from sample 1. Data for 5 are from sample 3.*

4. Discussion

4.1 Method considerations

Middle ear anatomy is described in many different standard textbooks, in more or less detail. Data are mainly based either on direct visual observation under the microscope or on histologic sections. 3D representations are mainly hand-made drawings to explain the principles of the structure, but such drawings do not contain numerical detail. As an example we refer to the standard work by Anson and Donaldson (1981), where fig. III-35 gives a detailed drawing of the ossicular chain, indicating the place of attachment or position of multiple ME ligaments and muscles.

4.1.1 Contrast-enhanced micro-CT as morphological imaging technique

Below, the advantages and disadvantages of micro-CT compared to other options for studying ME morphology (surgery, histology, magnetic resonance imaging (MRI), light sheet fluorescence microscopy (LSFM) (Buytaert et al., 2010) and optical coherence tomography (OCT) (Van der Jeught et al., 2013)) are listed. The reason for choosing stained micro-CT for this study is the combination of the mentioned benefits and the fact that our research lab has plenty of experience using the technique.

Advantages:

- Non-contact (vs. surgery);
- Non-destructive (vs. histology);
- Easy alignment of different sections (vs. histology);
- No need for bone decalcification (vs. histology);
- Isotropic voxel dimensions (vs. MRI and histology);
- Higher imaging resolution than MRI;

- Imaging of visually unavailable structures with great penetration depth (vs. OCT);
- Bone imaging without intensive and aggressive refractive index manipulation (vs. LSFM);

Disadvantages:

- No in-vivo measurements (vs. surgery and clinical CT);
- No tangible feedback during examination (vs. surgery and ex-vivo dissection);
- Worse specificity for soft-tissue than histology, optical microscopy, MRI and LSFM;
- Staining required (vs. surgery, optical microscope, MRI, OCT);
- Less imaging options than MRI (cfr. different sequences);
- Lower spatial resolution than histology, OCT and LSFM ;
- Longer scan time (increasing the risk of tissue deformation during measurement) than LSFM, which can be performed in real-time;
- Harmful radiation (for the operator), thus extensive safety measures required.

4.1.2 Segmentation operator bias

It has been argued during many review processes in the past that manual segmentation provides results that could be significantly dependent on the operator's subjective input. The influence of the operator on segmentation results has been quantified in Buytaert et al. (2014). The study concluded that the results of a manual segmentation process are only marginally dependent on the operator and that inter-operator repeatability is more than satisfactory, provided that good a-priori guidelines were agreed upon by the different operators.

4.2 Interpretation of Results and Comparison to Literature

Topic I: Influence of PTA on Ossicle Configuration

Potential tissue alteration caused by staining agents is a topic that should not be neglected in studies that rely on or provide new morphometric data. In Buytaert et al. (2014), the influence of different staining agents, including phosphotungstic acid (PTA), on the volume of different tissue types was investigated. The study concluded that PTA results in the least amount of shrinkage of the studied staining agents: bone exhibits even a negative volume shrinkage of (-1.3 $\pm$ 3.9) % (i.e. volume increase) after applying PTA staining, indicating a marginal effect; muscle tissue exhibits significant average volume shrinkage of (10.4 $\pm$ 2.6) % (i.e. linear shrinkage of 3.6%) after applying PTA staining.

From the results of the current study (see table 2), it is clear that the influence of the applied staining procedure on the ossicle configuration is very small and that the small alterations do not appear in a systematic manner. Indeed, the measured joint angle changes appear in different directions for different samples. Therefore, we can assume that other results of this study that use the spatial locations of the ossicles are not systematically altered in the same manner by the application of a staining agent, despite the fact that non-negligible soft-tissue shrinkage might have occurred, as investigated and shown in Buytaert et al. (2014).

Topic II: Middle Ear Ligaments

For the interpretation of the many abbreviations in this section, we refer the reader to tables 1 and 3. Our findings confirm that there are various possible sources of confusion and misinterpretation in identifying ME ligaments:

- Many mucosal strands could be easily interpreted as ligaments, and vice versa; this could be the case for the M-AML, the MIL (medial incudal ligament) and the SSL;
- Some ligaments (P-SML and M-AML) had remarkable variation in attachment point to the ossicular chain.

We hope to clear some of the confusion by a close comparison of similar ligaments in all of our samples and a subsequent application of a consistent nomenclature (see table 3).

In the context of middle ear morphology, the anterior mallear ligament (AML) is often treated as a single structure, attaching to the anterior process of the malleus and disappearing in the petrotympanic fissure. In literature on temporomandibular morphology, however, there is mention of two ligaments that originate from the temporomandibular joint region, travel through the petrotympanic fissure and finally attach to the anterior side of the malleus: the discomallear ligament (DML) and a separated branch of the sphenomandibular ligament (SpML) (Kim et al., 2004; Sencimen et al., 2008). The DML connects the malleus to the articular disc of the temporomandibular joint (Cheynet et al., 2003; Kim et al., 2004; Rowicki and Zakrzewska, 2006; Sencimen et al., 2008). The tympanic branch of the SpML, after passing through the petrotympanic fissure, is continuous with the sphenomandibular ligament (Sencimen et al., 2008). In 60-80% of the cases, these two ligaments are merged at the point of attachment to the malleus (Kim et al., 2004; Sencimen et al., 2008), which explains why they are often treated as one ligament in middle ear morphology and mechanics. Both ligaments pass through the petrotympanic fissure and are partially attached to it, limiting their influence on ossicular motion significantly. Only the tympanic branch of the SpML has been observed to induce observable motion in the ossicular chain after overstretching, which is denied for the DML in multiple studies (Kim et al., 2004; Sencimen et al., 2008).

In our micro-CT datasets, the distinction between the DML and the temporal branch of the SpML is not visible at their attachment to the malleus, although the attachment base surface of the combined structure is significantly larger than that of other ligaments, which is consistent with its compound nature. Anterior to the malleus, the combined structure enters the petrotympanic fissure, in which a thin bony wall is observed, that divides the petrotympanic fissure into two unequal compartments and through which the two ligaments separately run. In Figure 5, the combined shape of the DML and the tympanic branch of the SpML is captured by a single structure labeled AML.

The other most prominent ligament is the PIL. Together with the AML, the PIL defines the classic anatomical axis of ossicular rotation. Given their thickness and consistency in comparison to the other ME ligaments, we can only confirm their morphologic importance. However, we do not make any claims regarding ossicular motion, as this topic is indeed a debated subject (Cai et al., 2010; Puria and Steele, 2010), certainly at higher frequencies, and addressing of this topic should be reserved for dedicated papers.

It is debatable how important all the other ME ligaments are in terms of ossicular mechanics, given their limited thickness, inconsistent presence and attachment points, and the difficulty to distinguish them from the surrounding mucosal folds and strands. These mucosal folds, however, are sufficiently apparent, numerous and generally large (see Figure 5), to suggest that they could have a significant suspensory role in addition to their assumed contribution to ME gas exchange (Marcusohn et al., 2010) and blood supply to the ossicles (Sim and Puria, 2008).

The identification of the PML as mucosal folds attaching partially to the chorda tympani agrees with Gulya and Schuknecht (1995) in that they call it the posterior mallear fold, which envelopes the chorda tympani.

We plead for a consistent nomenclature of all observed ME ligaments. This could be debatable for the M-AMLand the P-SML, as they attach partially or even fully to the capsule of the IMJ in some samples. We propose to name them 'mallear ligament' despite this variation in location of attachment so that a clear communication of these structures is facilitated in future literature. Two incudomallear joint (IMJ) ligaments have been mentioned before (Gulya and Schuknecht, 1995; Lemmerling et al., 1997), namely a medial and a lateral IMJ ligament. These names, however, referred to the medial and lateral portions of the capsule of the IMJ. These joint structures are not included in this topic, but were observed in all samples. However, in one of the samples (sample 1), a ligament was observed that is continuous with the medial portion of the capsule of the IMJ and attaches to the cavity wall and the mastoid bone. This ligament has been named the medial incudomallear ligament (MIML) in table 3. In order to know whether this is a reoccurring structure in the human ME or rather an anomaly in said single sample, more data is needed.

To the authors' knowledge, no stapedial ligament, aside from the stapedial annular ligament (SAL), has ever been mentioned in literature. However, there was a clear thin ligamentous connection between the superior side of the stapes head and the cavity wall near the cochlea bone in one of the samples. The authors named it superior stapedial ligament (SSL) and regret to add yet another ligament to the already confusing list. The SAL is not covered in this topic, as it has a clearly different anatomic appearance and morphologic role than the other ME ligaments.

We did not identify a superior incudal ligament (SIL) in any of our samples, although this structure has been mentioned in literature (Federative Committee on Anatomical Terminology (FCAT), 1998; Mikhael, 2005). In Anson and Donaldson (1981) the PIL is described as "*a fold of mucous membrane that descends from the tympanic roof to the body of the incus"*. Such folds are indeed observed (see Figure 5), but were never identified as ligaments, and certainly not posterior but rather superior.

Topic III: Ossicle Parameters and Dimensions

In many current FE models of the ME, the ossicles are regarded as homogeneous structures with a single mass density value (Fay et al., 2006; Böhnke et al., 2013; De Greef et al., 2014). Sometimes different values are used for different parts of the ossicles, such as the arm, neck and head of the malleus (Kelly et al., 2003; Gan et al., 2006, 2009; Wang et al., 2007; Hoffstetter et al., 2010; Gentil et al., 2011, 2014). However, the ossicles are not completely solid, but contain internal blood vessels (Kirikae, 1960) and cavities containing connective tissue, for example at the distal end of the long process of the incus (Karmody et al., 2009). In this study, all non-bone tissue, as said earlier, was combined under the term 'intertrabecular spaces' and includes mostly blood vessels, but also collagen and cartilage, particularly at the distal end of the incus and at the head of the stapes (Chien et al., 2009; Karmody et al., 2009). Literature mentions the following mass density values for these materials:

- Blood: 1.06 g/ml (Cutnell and Johnson, 1999)
- Cartilage: 1.05 g/ml (Joseph et al., 1999); 1.06–1.18 g/ml (Alexander, 2003)
- Collagen: 1.16 g/ml at 95% humidity (Harley et al., 1977)

As the exact contribution ratios of these tissue types in the ossicles were unknown, we have chosen to use 1.06 g/ml as mass density for all intertrabecular spaces in the calculations. This way, the density difference with bone and therefore the influence of the lower density regions was certainly not underestimated.

Our results indicate statistically significant differences for some of the principal moments of inertia (PMI) of the ossicles between density cases 1 (homogeneous ossicles) and 2 (inhomogeneous). However, this does not necessarily imply a relevant impact on ME mechanics, which is a question that needs to be addressed using other tools than the ones in the current study.

For multiple reasons, the incudomallear complex is often treated as one mechanical unit. Fleischer (1978) points out that the alteration of the mass distribution of the incudomallear complex (IMC) is an effective way to tune the natural frequency f_n of the system, because of the following relation:

$$f_n = \frac{1}{2\pi}\sqrt{\frac{K}{\underbrace{I_0 + m_{\mathrm{IMC}}.\, d^2_{\mathrm{AnAx-COM}}}_{I_{tot}}}}, \tag{4}$$

where K denotes the stiffness of the rotational axis and I_{tot} the total moment of inertia of the IMC for rotation around the anatomical axis. According to the parallel axis theorem, I_{tot} is the sum of:

- I_0: the moment of inertia of the IMC around an axis parallel to the anatomical axis but through its COM; and
- $I_{\mathrm{AnAx-COM}} = m_{\mathrm{IMC}}.\, d^2_{\mathrm{AnAx-COM}}$: as defined in section 2.3.III.

Therefore, by altering $d^2_{\mathrm{AnAx-COM}}$, the natural frequency of the IMC can be effectively tuned to the species' evolutionary needs (Fleischer, 1978). The relative change in natural frequency is given by:

$$\begin{aligned}\Delta f_n &= \frac{f_{\mathrm{misaligned}} - f_{\mathrm{aligned}}}{f_{\mathrm{aligned}}} \\ &= \sqrt{\frac{I_0}{I_{tot}}} - 1\end{aligned} \tag{5}$$

where f_{aligned} and $f_{\mathrm{misaligned}}$ denote the natural frequencies calculated using equation (4) for respectively $d_{\mathrm{AnAx-COM}} = 0$ and the average $\langle d_{\mathrm{AnAx-COM}} \rangle$. The ratio $r_{\mathrm{eff}} = I_{\mathrm{AnAx-COM}}/I_{\mathrm{tot}}$ is a measure for the degree of efficiency loss due to the misalignment of the COM of the IMC with the anatomical rotation axis. A higher r_{eff} indicates a poorer efficiency for the rotation around the anatomical axis.

The results indicate that rotation around the anatomical rotation axis is not as efficient as it could be. If the IMC's COM would coincide with the anatomical axis, the moment of inertia would be (37 $\pm$ 7) % smaller. This result supports the suggestion that at higher frequencies the 'hinge-like' motion of the IMC becomes very inefficient (Cai et al., 2010; Puria and Steele, 2010). At these frequencies, the IMC does not move as a rigid body, but rather as a system with a flexible joint whose motion is better described by a 'bevel gear' motion (Cai et al., 2010; Puria and Steele, 2010). Furthermore, the current data suggests that the natural frequency of the IMC gets a relative downward shift of (21 $\pm$ 4) % due to the COM misalignment.

In Sim et al. (2007) the PMIs and principal axes of rotation (PAR) of the malleus, incus and IMC were determined through a similar method using micro-CT measurements. Their results for the PMIs are consistently slightly higher but the error bars of both studies overlap for all values. Notice that they used the standard error of the mean, which is by definition smaller than the corrected standard deviation, used in the current paper. Their determination of the PAR directions aligns with ours. They assumed the intertrabecular spaces to have the same mass density as water (i.e. 1000 kg/m^3), and determined the density of bone by physically weighing the ossicles.

In Puria and Steele (2010), micro-CT was employed as well to obtain shape and inertia data of the three separate ossicles. For comparative reasons, PMI results were normalized to the average density of the bones. No uncertainty data were reported. After normalizing our data to the densities as well, results agree very well with the current data, apart from the middle (I_2) and largest (I_3) PMI of the malleus, which are significantly higher in our data. The PAR directions of the ossicles were categorized in the same manner as in the current study, and the result of this was equal to our conclusions.

The shapes of the IMC and the stapes were calculated in Weistenhöfer and Hudde (1999) by recording their silhouettes under multiple angles. Subsequently, the PMIs and PARs were derived. No uncertainty intervals are mentioned, and their results were outside of our uncertainty intervals for 3 out of 6 parameters: I_2 and I_3 of the stapes (both higher than ours) and I_1 of the IMC (lower than ours). Their determination of the PAR directions is consistent with ours.

Finally, in Sim et al. (2013) inertia data for the stapes were published which were very different from our results. PMI values are normalized to the stapes mass, and their results of 0.47 mm^2 for the malleus, 1.00 mm^2 for the incus and 1.35 mm^2 for the stapes are very different from our results of respectively 0.688 mm^2, 1.457 mm^2 and 1.97 mm^2, even when taking into account the uncertainty of approximately 10% for both data. Furthermore, the *x*-axis (ant-post) was identified as the axis with the largest PMI, followed by the *y*-axis (sup-inf), which is contradictory to our findings, as well as those of Weistenhöfer and Hudde (1999) and Puria and Steele (2010).

For most measured ossicle dimensions we found values which overlap values reported in literature (table 7), although the match with Gan et al. (2002) is rather poor.

An interesting notion is that our ossicular lever arm length ratio of (1.3 ± 0.1) with respect to the anatomical axis produces a result which is very similar to the approximated approach from Hemila et al. (1995). Furthermore, our data are consistent with the ossicular morphometric data from Ars (1977).

Topic IV: Morphology of the Distal Incus

The nature and properties of the lenticular process has been the topic of study and controversy in multiple papers. Asheron (1978) provides a historical overview of the many claims that have been made regarding the existence of a fourth ossicle, named os orbiculare (Asherson, 1978) or os lenticularis (Hoffstetter et al., 2011), that would consist of the bony disk, forming the lateral articulating surface of the incudostapedial joint (ISJ). Pal'chun and Magomedov (1997) reported an extensive study involving 40 incus samples from which was concluded that the lenticular process is a separate bone that is merely connected to the incus by a dense partially developed connective tissue. Chien et al. (2009) performed an even more extensive study, involving histology on 108

specimens, and disagreed fundamentally with Pal'chun and Magomedov (1997). Chien et al. (2009) attribute the different conclusions to discrepancies in tissue dissection, tissue embedding, orientation of the sections and tissue identification. The images of the freely available histologic image library at http://otopathologynetwork.org/educational-resources/atlas/, provided by the Massachusetts Eye and Ear Infirmary, suggest that the pedicle of the lenticular process mainly consists of cartilage and underdeveloped bone, based on the absence of osteons in the incudal tissue. This is however based on a single individual, so general insights and inter-individual variability cannot be deducted from these data.

It is suggested in Graboyes et al. (2011) that one of the main sources of confusion may be the lack of widely accepted nomenclature regarding the distal end of the incus: the 'fourth ossicle' itself has been known under different names and the definition of the term lenticular process has been subject to inconsistency as well.

Another possible source of inconsistency is the fact that the delicate anatomical features of the distal incus are very difficult to incorporate in simulations of ME mechanics and are therefore often neglected. Nevertheless, as stressed by Decraemer and Khanna (2004), Funnell et al. (2005) and more recently Chien et al. (2009), the curious anatomy could very well have considerable implications for the mechanics of the ISJ. They argue that the thin pedicle may bend during ossicular motion, "*thereby adding flexibility to the ISJ and reducing the transmission of particular motion components from the incus to the stapes*." (Chien et al., 2009)

The technique used in the current study does not allow identification of the soft tissue type, but as elaborated above, this has been studied in other papers (Chien et al., 2009; Karmody et al., 2009) through histology, which is a more suitable technique for this purpose. It is, however, possible to assess the properties of the bony core of the distal incus (table 8). In our datasets, the pedicle of the lenticular process is nowhere interrupted, undermining the existence of a separate 'fourth ossicle'. This is consistent with the most recent studies on this topic (Chien et al., 2009; Karmody et al., 2009). The quantitative width data are rather inconsistent with the findings of Chien et al. (2009), who reported that the diameter of the pedicle is (260 $\pm$ 104) μm, while our result is (385 $\pm$ 92) μm. Both studies however confirm a very large inter-individual variety in structural anatomy.

The micro-CT data cannot distinguish between bone and strongly calcified cartilage. According to Mente and Lewis (1994), the difference in elastic modulus between these tissue types is one order of magnitude. Therefore this distinction is very important: if the pedicle consists mostly of cartilage, the "bending" theory of Decraemer and Khanna (2004) and Funnell et al. (2005) gathers more credibility, while a stiff bony connection would undermine it. It is clear that more knowledge and consensus on the mechanical parameters of this feature are still needed.

Topic V: TM and stapes footplate Areas

In the literature, many data can be found on either TM and SFP surface areas, both 2D projected areas and real 3D areas, or measurements of ellipse short and long axis lengths. Table 13 and Figure 12 provide overviews of different literature values. When only axis lengths were reported, we have calculated the approximated ellipse surface area to compare with our results. All literature values lie within or very close to the uncertainty range of the current study (i.e. average ± standard deviation).

Table 13. *Comparison of our results for the TM and SFP surface areas and the hydraulic area ratio to published data. If mentioned, the method used in the cited study is included. Some values are derived by the authors from other values in the referred source. A dash (-) between two values denotes the range of values, rather than an uncertainty interval. Otherwise, a sole dash represents absent data. Figure 12 provides a visual representation of this comparison. References: (Wever and Lawrence, 1954; Kirikae, 1960; Ars, 1977; Molvaer et al., 1978; Rosowski, 1994; Hemila et al., 1995; Nummela, 1995; Stenfelt et al., 2004; Gan et al., 2006; Schraven et al., 2011; Salih et al., 2012; Sim et al., 2013).*

Source	Method	TM Area (mm^2)	SFP Area (mm^2)	Ratio
De Greef 2015	**Ellipse**	**57,6 ± 7,0**	**2,80 ± 0,20**	**20,6 ± 2,1**
	2D Proj	**59,4 ± 6,9**	**3,04 ± 0,17**	**19,6 ± 2,3**
	3D Surf	**65,6 ± 5,6**	**3,26 ± 0,19**	**20,2 ± 2,1**
Kirikae 1960	Ellipse	-	3,09 [1]	-
	2D Proj	55,4 ± 4,5	-	17,9 [1]
	3D Surf	57 - 64 [2]	-	-
Ars 1977	Ellipse	59	-	-
Nummela 1995	Ellipse	68,3	-	-
Hemila 1995	Ellipse	68,3	2,98	22,9 [1]
Rosowski 1994	Literature[3]	60	3,2	18,8 [1]
	Theoretical fit	-	-	20
Stenfelt 2004	2D Proj	-	3,85 (3 - 5,3) [2]	-
Gan 2006	3D Surf	72 [1]	-	-
Schraven 2011	Unmentioned	-	3,2	-
Salih 2012	Unmentioned	-	3,16 - 4,09 [2]	-
Sim 2013	2D Proj	-	2,86 ± 0,32	-
	3D Surf		3,03 ± 0,33	

[1] Value derived by authors

[2] Range of values

[3] Wever and Lawrence 1954; Molvaer 1978

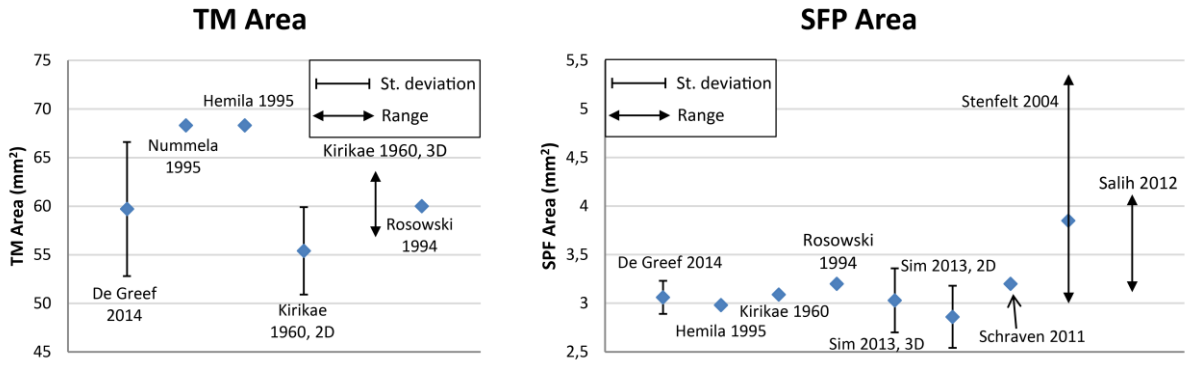

Figure 12. *Literature comparison of published values for the TM and SFP surface areas.*

The question whether the 2D projection method or the 3D projected area method provides the most relevant measure for sound collection is a difficult topic in which the complicated interplay between acoustics and biomechanics needs to be considered. Therefore, we leave these further considerations for dedicated studies.

Topic VI: Thickness of Different Structures

The thickness of the TM has been the subject of study in multiple papers, yet even the most recent ones (Kuypers et al., 2006; Van der Jeught et al., 2013) conclude that more statistical data are needed to make final conclusions. The current data (table 10) are a useful contribution, but should be interpreted with awareness about the possible effect of the applied staining with regard to tissue shrinkage. Nevertheless, the distribution of thickness and the correlation of its statistical properties to other ME dimensions, as suggested by other authors, can be a valuable addition to existing data.

Our findings for the average TM thickness ((81 $\pm$ 18) μm, range 59.1 – 105.7) are consistent with literature values of 77.93 – 91.76 μm (Van der Jeught et al., 2013), 40 – 120 μm (Kuypers et al., 2006), 64 – 95 μm (Schmidt and Hellström, 1991), 30-90 μm (Lim, 1970) and 20 – 430 μm (Ruah et al., 1991), although the ranges of uncertainty differ significantly between different authors. No correlation between the average TM thickness and the inferior-superior length of the TM was observed, in contradiction to (Van der Jeught et al., 2013).

The IMJ features an excessive bulge at a medio-superior location (see table 11). Presumably, this bigger space between the ossicles allows for a larger attachment surface of the IMJ capsule, consisting mainly of elastic fibers (Willi, 2003). Apart from the area of the bulge, the location of maximal thickness is not consistent, while the thinnest region of the IMJ is consistently located at a lateral or latero-superior position. The mean minimal thickness is consistent with the findings of Sim and Puria (2008), reporting (0.04 $\pm$ 0.005) mm for the mean minimal thickness. Their result for the mean maximal IMJ thickness of (0.32 $\pm$ 0.029) mm is significantly different from ours. The mentioned study used another thickness calculation algorithm and did not exclude the medio-superior bulge from the assessment of maximal thickness.

The ISJ is more regular and flat than the IMJ space (see table 11). The location of minimal thickness is inconsistent between samples, but the maximal thickness is located posteriorly in 5 out of 6 samples.

In 4 out of 6 samples, the stapedial annular ligament (SAL) is unresolvable at multiple places, resulting in an observed thickness of 0 μm (see table 12). This is probably caused by volume averaging artifacts in the micro-CT reconstruction, given the relatively large voxel sizes (voxel pitches of 22.8 μm (samples 1, 3-6) and 18.5 μm (sample 2)) compared to the thickness of the SAL. The maximal thickness of the SAL is consistently located anteriorly or antero-inferiorly. Sim et al. (2013) performed high-resolution micro-CT measurements on separated stapes samples, enabling a smaller voxel size than in the current study. In that study, no places were reported where the SAL thickness decreased to 0.

Finally, the round window (RW) of the cochlea did not feature consistent locations for either the maximal nor the minimal thickness (see table 12).

As discussed earlier, we should acknowledge that these thickness results could be slightly inaccurate due to PTA-induced tissue shrinkage, although this effect can be expected to be minor, as a linear shrinkage of only 3.6 % is reported in Buytaert et al. (2014) for muscle tissue.

4.3 Relevance of Morphological Data for ME modeling

An important application of high-resolution 3D morphological data of the ME is finite element (FE) modeling. The quality and complexity of FE models continue to improve with the availability of increasingly more computational resources. Some small soft tissue structures with complicated mechanical properties are challenging to incorporate in these models, and different approaches have been taken in published models. For instance, in Gan et al. (2009), all ligaments that were found in the sample that was used for shape data were incorporated using the experimentally acquired shape data. In other recent models, however, the ligaments are represented by either simple geometric shapes (Gentil et al., 2014) or by mechanical elements such as Voight elements (Böhnke et al., 2013). It is however possible that some experimental features of ME functionality, such as the relative flatness of the ME's frequency response function over a broad frequency range, cannot be predicted using these hybrid models. The distributed nature of the ME density, stiffness and other parameters, could be the underlying reason for some of these features. Therefore, it is valuable to continue to make efforts to minimize all possible sources of differences between modeling and experimental outcomes, including low-resolution image data or lumped-parameter elements. The new morphological data presented in this paper could be valuable in the advancements of this effort.

4.4 Conclusions and Summary

In this study, multiple topics of ME morphology have been studied by means of segmentation and interpretation of six micro-CT datasets of PTA-stained human temporal bones. Segmentation was done using a combination of automatic and manual segmentation tools. Statistical results have been extracted for all topics. The influence of the PTA staining on the spatial configuration of the ossicles has been demonstrated to be negligible. The following conclusions have been drawn:

- Ligaments (see table 3): The AML, LML, PML and PIL were present in all samples, although the PML was not identified as a ligament. The M-AML, S-AML, A-SML, P-SML, MIML, MIL, LIL and ASL were observed in at least one but not in all samples.
- The COMs, PMIs and PARs of all ossicles and the IMC were calculated and compared against literature data. We revealed a statistically significant influence of the incorporation of ossicle inhomogeneities on some ossicle inertia parameters. Some linear ossicle dimensions were measured and evaluated as well, including the distances that define the ossicular lever arm ratio. This ratio was found to be (1.30 ± 0.11).
- The distal portion of the incus featured an inconsistently shaped bony connection between the long process of the incus and the lenticular process. This pedicle had a mean maximal width of (385 ± 92) µm and its mean thickness was (54 ± 20) µm and was surrounded by a large amount of soft tissue, yet was nowhere interrupted.
- The surface areas of both TM and SFP have been measured in three different manners (ellipse approximation, 2D projection and 3D surface). For the 2D projection method, the mean TM area was found to be (59.4 ± 6.9) mm², for the SFP this was (3.04 ± 0.17) mm². The mean TM/SFP area ratio was (19.6 ± 2.3).

- The mean TM thickness was (80 ± 18) μm, ranging from 59 μm to 106 μm. The TM thickness distribution of our samples did not suggest consistent local thickening of the membrane in certain quadrants and no correlation between the mean TM thickness and the inferior-superior TM length has been found. The IMJ consistently featured an excessively thick bulge at its medio-superior portion with a thickness of (983 ± 88) μm and apart from this a mean thickness minimum of (35 ± 20) μm and a mean maximum thickness of (235 ± 20) μm, with the thinnest point consistently located laterally. For the ISJ this was (78 ± 20) μm and (163 ± 45) μm (consistently posterior), for the SAL (6 ± 20) μm and (290 ± 60) μm (consistently anterior), and for the RW (55 ± 20) μm and (221 ± 39) μm (no consistent locations).

Author contributions

Daniël De Greef is the first author and main writer of this paper; his contribution included manual segmentation of micro-CT datasets, post-processing and interpreting the datasets to retrieve the values of interest, performing literature study on all topics and writing the manuscript. Jan Buytaert had an equal contribution, except for the writing of the manuscript. Johan Aerts has prepared the samples for micro-CT scans and he carried out most of the early-stage segmentation work. Luc Van Hoorebeke and Manuel Dierick have developed the micro-CT setup and carried out the actual micro-CT scans of all samples. Joris Dirckx is supervisor of the first three authors and was involved in many interpretational and strategic decisions.

Acknowledgements

This research was funded by the Research Foundation – Flanders (FWO) and the Agency for Innovation by Science and Technology (IWT). We thank Jean-Marc Gerard from the Cliniques Universitaires Saint-Luc (UCL) and Cochlear Technology Centre Belgium for providing the needed human specimens for this study.

References

Aernouts J, Aerts JRM, Dirckx JJJ. 2012. Mechanical properties of human tympanic membrane in the quasi-static regime from in situ point indentation measurements. Hear Res 290:45–54.

Alexander R. 2003. Principles of animal locomotion. Princeton, NJ: Princeton University Press.

Anson BJ, Donaldson JA. 1981. Surgical Anatomy of the Temporal Bone. Third. ed. New York: Raven Press.

Ars B. 1977. Bijdrage tot de heelkundige anatomie van het tympano-ossiculaire systeem. Acta Otorhinolaryngol Belg 31:50–68.

Asherson N. 1978. The fourth auditory ossicle: fact or fantasy? J Laryngol Otol 92:453–465.

Böhnke F, Bretan T, Lehner S, Strenger T. 2013. Simulations and Measurements of Human Middle Ear Vibrations Using Multi-Body Systems and Laser-Doppler Vibrometry with the Floating Mass Transducer. Materials (Basel) 6:4675–4688.

Buytaert J a. N, Adriaens D, Dirckx JJJ. 2010. Orthogonal-plane fluorescence optical sectioning: a technique for 3-D imaging of biomedical specimens. ArchiveUgentBe 1356–1365.

Buytaert J, Goyens J, De Greef D, Aerts P, Dirckx J. 2014. Volume Shrinkage of Bone, Brain and Muscle Tissue in Sample Preparation for Micro-CT and Light Sheet Fluorescence Microscopy (LSFM). Microsc Microanal 20:1208–1217.

Cai H, Jackson RP, Steele CR, Puria S. 2010. A Biological Gear in the Human Middle Ear. In: Proceedings of the COMSOL Conference.

Cheynet F, Guyot L, Richard O, Layoun W, Gola R. 2003. Discomallear and malleomandibular ligaments: anatomical study and clinical applications. Surg Radiol Anat 25:152–157.

Chien W, Northrop C, Levine S, Pilch BZ, Peake WT, Rosowski JJ, Merchant SN. 2009. Anatomy of the distal incus in humans. J Assoc Res Otolaryngol 10:485–496.

Cutnell JD, Johnson KW. 1999. Physics. Fifth. ed. Wiley.

De Greef D, Aernouts J, Aerts J, Cheng JT, Horwitz R, Rosowski JJ, Dirckx JJJ. 2014. Viscoelastic properties of the human tympanic membrane studied with stroboscopic holography and finite element modeling. Hear Res 312:69–80.

Decraemer WF, Khanna S. 2004. Measurement, visualization and quantitative analysis of complete three-dimensional kinematical data sets of human and cat middle ear. In: Wada H, editor. Proceedings of the 3rd Symposium on Middle Ear Mechanics in Research and Otology Singapore: World Scientific. p. 3–10.

Fay JPJP, Puria S, Steele CR. 2006. The discordant eardrum. Proc Natl Acad Sci U S A 103:19743–19748.

Federative Committee on Anatomical Terminology (FCAT). 1998. Terminologica Anatomica: International Anatomical Terminology. Stuttgart: Thieme.

Fleischer G. 1978. Evolutionary principles of the mammalian middle ear. Adv Anat Embryol Cell Biol.

Funnell WRJ, Heng Siah T, McKee MD, Daniel SJ, Decraemer WF. 2005. On the coupling between the incus and the stapes in the cat. J Assoc Res Otolaryngol 6:9–18.

Funnell WRJ, Laszlo CA. 1978. Modeling of the cat eardrum as a thin shell using the method. J Acoust Soc Am 63:1461–1467.

Funnell WRJ, Medical B. 1983. On the undamped natural frequencies and mode shapes of a finite-element. J Acoust Soc Am 73:1657–1661.

Gan RZ, Cheng T, Dai C, Yang F, Wood MW. 2009. Finite element modeling of sound transmission with perforations of tympanic membrane. J Acoust Soc Am 126:243–253.

Gan RZ, Sun Q, Dyer RK, Chang K-H, Dormer KJ. 2002. Three-dimensional Modeling of Middle Ear Biomechanics and Its Applications. Otol Neurotol 23:271–280.

Gan RZ, Sun Q, Feng B, Wood MW. 2006. Acoustic-structural coupled finite element analysis for sound transmission in human ear--pressure distributions. Med Eng Phys 28:395–404.

Gan RZ, Wang X. 2014. Modeling Microstructure of Incudostapedial Joint and the Effect on Cochlear Input Finite Element Modeling of ISJ Microstructure. In: Mechanics of Hearing Proceedings Cape Sounio.

Gentil F, Garbe C, Parente M, Martins P, Ferreira A, Jorge RN, Santos C, Paço J. 2014. Analysis of Eardrum Pathologies Using the Finite Element Method. J Mech Med Biol 14:1450034.

Gentil F, Parente M, Martins P, Garbe C, Jorge RN, Ferreira A, Tavares JMRS. 2011. The influence of the mechanical behaviour of the middle ear ligaments: a finite element analysis. Proc Inst Mech Eng P 225:68–76.

Graboyes EM, Hullar TE, Chole RA. 2011. The lenticular process of the incus. Otol Neurotol 32:1600–1604.

Gulya AJ, Schuknecht HF. 1995. Anatomy of the temporal bone with surgical implications. Parthenon Pub. Group.

Harley R, James D, Miller A, White JW. 1977. Phonons and the elastic moduli of collagen and muscle. Nature 267:285–287.

Hemila S, Nummela S, Reuter T. 1995. What middle ear parameters tell about impedance matching and high frequency hearing. Hear Res 85:31–44.

Hoffstetter M, Lugauer F, Kundu S, Wacker S, Perea-Saveedra H, Lenarz T, Hoffstetter P, Schreyer AG, Wintermantel E. 2011. Middle ear of human and pig: a comparison of structures and mechanics. Biomed Tech (Berl) 56:159–165.

Hoffstetter M, Schardt F, Lenarz T, Wacker S, Wintermantel E. 2010. Parameter study on a finite element model of the middle ear. Biomed Eng (NY) 55:19–26.

Joseph D, Gu W, Mao X, Lai W, Mow V. 1999. True density of normal and enzymatically treated bovine articular cartilage. Trans Orthop Res Soc 24:642.

Karmody CS, Northrop CC, Levine SR. 2009. The incudostapedial articulation: new concepts. Otol Neurotol 30:990–997.

Kelly DJ, Prendergast PJ, Blayney a W. 2003. The effect of prosthesis design on vibration of the reconstructed ossicular chain: a comparative finite element analysis of four prostheses. Otol Neurotol 24:11–19.

Kim HJ, Jung HS, Kwak HH, Shim KS, Hu KS, Park HD, Park HW, Chung IH. 2004. The discomallear ligament and the anterior ligament of malleus: an anatomic study in human adults and fetuses. Surg Radiol Anat 26:39–45.

Kirikae I. 1960. The structure and Function of the Middle Ear. University of Tokyo Press.

Kuypers LC, Decraemer WF, Dirckx JJJ. 2006. Thickness distribution of fresh and preserved human eardrums measured with confocal microscopy. Otol Neurotol 27:256–264.

Lemmerling MM, Stambuk HE, Mancuso a a, Antonelli PJ, Kubilis PS. 1997. CT of the normal suspensory ligaments of the ossicles in the middle ear. Am J Neuroradiol 18:471–477.

Lim DJ. 1970. Human Tympanic Membrane: An Ultrastructural Observation. Acta Otolaryngol 70:176–186.

Marcusohn Y, Ar A, Dirckx JJJ. 2010. Perfusion and diffusion limitations in middle ear gas exchange: the exchange of CO2 as a test case. Hear Res 265:11–14.

Masschaele BC, Cnudde V, Dierick M, Jacobs P, Van Hoorebeke L, Vlassenbroeck J. 2007. UGCT: New X-ray radiography and tomography facility. Nucl Instruments Methods Phys Res Sect A Accel Spectrometers, Detect Assoc Equip 580:266–269.

Mente PL, Lewis JL. 1994. Elastic modulus of calcified cartilage is an order of magnitude less than that of subchondral bone. J Orthop Res 12:637–647.

Mikhael C. 2005. Finite-Element Modelling of the Human Middle Ear. McGill University.

Molvaer OI, Vallersnes FM, Kringlebotn M. 1978. The size of the middle ear and the mastoid air cell. Acta Otolaryngol 85:24–32.

Muyshondt P, De Greef D, Soons J, Dirckx JJJ. 2014. Optical techniques as validation tools for finite element modeling of biomechanical structures, demonstrated in bird ear research. In: AIP Conference Proceedings 1600 Ancona. p. 330–337.

Nummela S. 1995. Scaling of the mammalian middle ear. Hear Res 85:18–30.

Pal'chun V, Magomedov M. 1997. Some anatomical features of the long process of the incus. Vestn Otorinolaringol 2:19–20.

Puria S, Steele C. 2010. Tympanic-membrane and malleus-incus-complex co-adaptations for high-frequency hearing in mammals. Hear Res 263:183–190.

Quam RM, Coleman MN, Martínez I. 2014. Evolution of the auditory ossicles in extant hominids: metric variation in African apes and humans. J Anat 225:167–196.

Rosowski JJ. 1994. Outer and middle ears. In: Comparative hearing: mammals Springer New York. p. 172–247.

Rowicki T, Zakrzewska J. 2006. A study of the discomalleolar ligament in the adult human. Folia Morphol (Warsz) 65:121–125.

Ruah CB, Schachern P a, Zelterman D, Paparella MM, Yoon TH. 1991. Age-related morphologic changes in the human tympanic membrane. A light and electron microscopic study. Arch Otolaryngol Head Neck Surg 117:627–634.

Salih WHMW, Buytaert JANAN, Aerts JRM, Vanderniepen P, Dierick M, Dirckx JJJJ. 2012. Open access high-resolution 3D morphology models of cat, gerbil, rabbit, rat and human ossicular chains. Hear Res 284:1–5.

Sanjay KK, Muthukumar R, Balasubramanian T. 2012. Endoscopic Tympanomastoid Exploration. Otolaryngol Online J 2.

Schmidt S-H, Hellström S. 1991. Tympanic-Membrane Structure – New Views. ORL J Otorhinolaryngol Relat Spec 53:32–36.

Schraven SP, Hirt B, Gummer AW, Zenner H-P, Dalhoff E. 2011. Controlled round-window stimulation in human temporal bones yielding reproducible and functionally relevant stapedial responses. Hear Res 282:272–282.

Sencimen M, Yalçin B, Doğan N, Varol A, Okçu KM, Ozan H, Aydintuğ YS. 2008. Anatomical and functional aspects of ligaments between the malleus and the temporomandibular joint. Int J Oral Maxillofac Surg 37:943–947.

Sim JH, Puria S. 2008. Soft tissue morphometry of the malleus-incus complex from micro-CT imaging. J Assoc Res Otolaryngol 9:5–21.

Sim JH, Puria S, Steele C. 2007. Calculation of inertial properties of the malleus-incus complex from micro-CT imaging. J Mech Mater Struct 2:1515–1524.

Sim JH, Röösli C, Chatzimichalis M, Eiber A, Huber AM. 2013. Characterization of stapes anatomy: investigation of human and Guinea pig. J Assoc Res Otolaryngol 14:159–173.

Stenfelt S, Hato N, Goode RL. 2004. Fluid volume displacement at the oval and round windows with air and bone conduction stimulation. J Acoust Soc Am 115:797.

Todd NW, Creighton FX. 2013. Malleus and incus: correlates of size. Ann Otol Rhinol Laryngol 122:60–65.

Unur E, Ulger H, Ekinci N. 2002. Morphometrical and morphological variations of middle ear ossicles in the newborn. Erciyes Med J 24:57–63.

Van der Jeught S, Dirckx JJJ, Aerts JRM, Bradu A, Podoleanu AGH, Buytaert J a N. 2013. Full-field thickness distribution of human tympanic membrane obtained with optical coherence tomography. J Assoc Res Otolaryngol 14:483–494.

Volandri G, Di Puccio F, Forte P, Carmignani C. 2011. Biomechanics of the tympanic membrane. J Biomech 44:1219–1236.

Volandri G, Di Puccio F, Forte P, Manetti S. 2012. Model-oriented review and multi-body simulation of the ossicular chain of the human middle ear. Med Eng Phys 34:1339–1355.

Wada H, Metoki T, Kobayashi T. 1992. Analysis of dynamic behavior of human middle ear using a finite-element method. J Acoust Soc Am 92:3157–3168.

Wang X, Cheng JT, Gan RZ. 2007. Finite-element analysis of middle-ear pressure effects on static and dynamic behavior of human ear. J Acoust Soc Am 122:906–917.

Weistenhöfer C, Hudde H. 1999. Determination of the shape and inertia properties of the human auditory ossicles. Audiol Neurootol 4:192–196.

Wever EG, Lawrence M. 1954. Physiological Acoustics. Princeton, N.J.: Princeton Univ. Press.

Willi UB. 2003. Middle ear mechanics: The dynamic behavior of the incudo-malleolar joint and its role during the transmission of sound. Universität Zürich.

Williams KR, Lesser TH. 1990. A finite element analysis of the natural frequencies of vibration of the human tympanic membrane. Part I. Br J Audiol 24:319–327.

Zhao F, Koike T, Wang J, Sienz H, Meredith R. 2009. Finite element analysis of the middle ear transfer functions and related pathologies. Med Eng Phys 31:907–916.